JOURNAL OF PETROLOGY | VOLUME 47 | NUMBER 5 | PAGES 1017–1050 | 2006 | doi:10.1093/petrology/egl003

The Role of Lithospheric Mantle Heterogeneity in the Generation of Plio-Pleistocene Alkali Basaltic Suites from NW Harrat Ash Shaam (Israel)

Y. WEINSTEIN[1,2]*, O. NAVON[3], R. ALTHERR[4] AND M. STEIN[3]†

[1]DEPARTMENT OF GEOGRAPHY, BAR-ILAN UNIVERSITY, RAMAT-GAN 52900, ISRAEL

[2]DEPARTMENT OF GEOCHEMISTRY, CENTER OF EARTH SCIENCE, UNIVERSITY OF GÖTTINGEN, 37077 GÖTTINGEN, GERMANY

[3]INSTITUTE OF EARTH SCIENCES, THE HEBREW UNIVERSITY OF JERUSALEM, JERUSALEM 91904, ISRAEL

[4]INSTITUTE OF MINERALOGY, UNIVERSITY OF HEIDELBERG, D-69120 HEIDELERG, GERMANY

RECEIVED AUGUST 9, 2004; ACCEPTED JANUARY 11, 2006
ADVANCE ACCESS PUBLICATION MARCH 7, 2006

Plio-Pleistocene volcanism in the Golan and Galilee (northeastern Israel) shows systematic variability with time and location: alkali basalts were erupted in the south during the Early Pliocene, whereas enriched basanitic lavas erupted in the north during the Late Pliocene (Galilee) and Pleistocene (Golan). The basalts show positive correlations in plots of ratios of highly to moderately incompatible elements versus the concentration of the highly incompatible element (e.g. Nb/Zr vs Nb, La/Sm vs La) and in diagrams of REE/HFSE (rare earth elements/high field strength elements) vs REE concentration (e.g. La/Nb vs La). Some of these correlations are not linear but upward convex. $^{87}Sr/^{86}Sr$ ratios vary between 0·7031 and 0·7034 and correlate negatively with incompatible element concentrations and positively with Rb/Sr ratios. We interpret these observations as an indication that the main control on magma composition is binary mixing of melts derived from two end-member mantle source components. Based on the high Sr/Ba ratios and negative Rb anomalies in primitive mantle normalized trace element diagrams and the moderate slopes of MREE–HREE (middle REE–heavy REE) in chondrite-normalized diagrams, we suggest that the source for the alkali basaltic end-member was a garnet-bearing amphibole peridotite that had experienced partial dehydration. The very high incompatible element concentrations, low K content, very low Rb contents and steep MREE–HREE patterns in the basanites are attributed to derivation from amphibole- and garnet-bearing pyroxenite veins. It is suggested that the veins were produced via partial melting of amphibole peridotites, followed by complete solidification and dehydration that effectively removed Rb and K. The requirement for the presence of amphibole limits both sources to lithospheric depths. The spatial geochemical variability of the basalts indicates that the lithosphere beneath the region is heterogeneous, composed of vein-rich and vein-poor domains. The relatively uniform $^{143}Nd/^{144}Nd$ ($\varepsilon Nd = 4{\cdot}0$–$5{\cdot}2$) suggests that the two mantle sources were formed by dehydration and partial melting of an originally isotopically uniform reservoir, probably as a result of a Paleozoic thermal event.

KEY WORDS: *basanites; lithospheric heterogeneity; magma mixing; amphibole peridotite; pyroxenites*

INTRODUCTION

Alkali basalts form a small part of the global basaltic inventory. However, the association with continental rift environments and the rich assemblages of mantle xenoliths they carry make them an important source of information on the composition of the uppermost mantle beneath continental areas and on the mechanisms of basaltic magma generation. A longstanding discussion concerns the question of whether continental alkali basalts are derived from asthenospheric or lithospheric mantle sources or a mixture of both (e.g. Altherr *et al.*, 1990; Wilson & Downes, 1991; Stein & Hofmann, 1992;

*Corresponding author. Telephone: 972-54-520-4873. Fax: 972-3-534-4430. E-mail: weinsty@mail.biu.ac.il
†Present address: Geological Survey of Israel, Jerusalem, Israel.

Stein *et al.*, 1997; Shaw *et al.*, 2003). Another discussion concerns the mechanism of melting, either a passive, extension-related scenario (e.g. Chapin, 1979; Bohannon *et al.*, 1989; Stein & Hofmann, 1992; Bradshaw *et al.*, 1993; Shaw *et al.*, 2003), or an active scenario, which involves a thermal anomaly, usually a mantle plume (e.g. Gass, 1970; White & McKenzie, 1989; Camp & Roobol, 1992; Wilson & Patterson, 2001). A third possibility, which involves melting of the lithosphere by heat conduction from a sub-lithospheric source, was discussed in the case of small-volume continental flood basalts (Turner *et al.*, 1996; following Gallagher & Hawkesworth, 1992), but is also relevant to the generation of alkali basalts, as discussed below.

A third question, which is closely related to the above two, concerns the involvement of fluids in the generation of alkali basalts. Hydrous fluids are known to be important in the subduction environment, where they control the degree of melting (e.g. Stolper & Newman, 1994). There is growing evidence that hydrous minerals are also a common constituent in the source rocks of continental alkaline lavas (e.g. Francis & Ludden, 1995), but the role of 'wet melting' in the petrogenesis of alkali basalts has still not been well established. For instance, the origin of both East African and western Arabian basalts is mainly discussed in terms of melting a dry peridotitic source (e.g. White & McKenzie, 1989; Camp & Roobol, 1992). Stein *et al.* (1997) were the first to consider the possibility that the presence of hydrous minerals (i.e. amphibole) in the lithospheric mantle, metasomatic remnants of Late Proterozoic subduction, may actually be the main control on partial melting beneath Arabia. Similarly, Späth *et al.* (2001) considered dehydration of a metasomatized lithosphere as the cause for melting under the Chyulu Hills, southern Kenya.

In this study we report the temporal and spatial variations in bulk-rock chemical and Nd–Sr isotopic composition of Plio-Pleistocene alkali basalts from the northwestern part of Harrat ash Shaam, one of the largest volcanic provinces in the Arabian plate (Fig. 1). We show that most of the variability in the trace element composition of these basalts cannot be accommodated by simple models of variable degree melting of a homogeneous mantle source. Instead, we attribute this variability to mixing of melts derived from partial melting of pyroxenite veins and their hydrated host peridotites. We also suggest that the veins were produced during earlier magmatic processes within the lithosphere. Finally, we discuss the implication of the model for the melting regime beneath northern Arabia.

Geological background

This study focuses on basalts that erupted during the Plio-Pleistocene in the Golan and the Galilee areas of northern Israel, which are located at the northwestern part of Harrat ash Shaam, the largest of about 20 Cenozoic volcanic fields in the western Arabian Peninsula (Fig. 1). The volcanism in Arabia is Oligocene to Holocene in age (31 Ma to recent; Menzies *et al.*, 1997; although ages as old as Middle Eocene have also been reported, e.g. Pallister, 1987), and is associated with rifting along the Red Sea. Volcanism in the Harrat ash Shaam commenced at about 25 Ma (Barberi *et al.*, 1980; Ilani *et al.*, 2001) and continued to recent times (Dubertret, 1955). At its northwestern edge, the Ash Shaam volcanic field is bisected by the Dead Sea Transform fault (Fig. 1), which separates the volcanism of the Galilee to the west from that of the Golan to the east. Volcanism in this area occurred in two main periods: Middle Miocene (17–9 Ma) and Plio-Pleistocene (5·5 Ma to recent, Mor, 1993; Shaliv, 1991). The center of the Middle Miocene volcanism is located in the Yizre'el Valley and southeastern Galilee (Fig. 1, Shaliv, 1991; Weinstein, 2000). The Plio-Pleistocene volcanism includes basaltic flows and cinder cones in the Golan and the eastern Galilee as well as basalts along the Dead Sea Transform. The latter are mostly known from subsurface drilling and are intercalated with lacustrine sediments (Mittlefehldt & Slager, 1986). This study focuses on the Plio-Pleistocene basalts from the Golan and Galilee.

Overall in the study area, there is a trend of decreasing age from south to north (e.g. Mor, 1993; Heimann *et al.*, 1996; Fig. 1). West of the Dead Sea Transform, the focus of the Middle Miocene volcanism was in the Yizre'el Valley, locally reaching a thickness of more than 800 m. Early Pliocene activity was concentrated in eastern Lower Galilee (west of the Sea of Galilee), and Late Pliocene lavas erupted further north, in the Upper Galilee (Fig. 1). The thickness of the Galilee Pliocene volcanic sections usually does not exceed 100 m. East of the Dead Sea Transform, the southern Golan plateau is covered by a 20–200 m section of Early Pliocene basalts (Fig. 1). Further north, in the Yahudiya plateau of the central western Golan, there is an ~150 m thick Late Pliocene basaltic section. This section is probably underlain in the subsurface by Early Pliocene basalts, as indicated by a 3·3 Ma basaltic flow in the bottom of one of the local canyons (sample Wy-292, Table 1) and from seismic reflection profiles (Dafny *et al.*, 2003). Pleistocene basalts are found only in the eastern and northern Golan (Fig. 1). In most of the eastern and northern Golan, the volcanic section is relatively thick (up to 700 m in the Bashanit area; Dafny *et al.*, 2003; Fig. 1), but the age of the subsurface volcanic rocks is not known (there is one small exposure of Early Pliocene basalts in the northernmost part of the Golan; Heimann *et al.*, 1996). A similar decreasing age pattern is observed along the Dead Sea Transform. Basalts beneath and around the Sea of Galilee are of Early Pliocene age

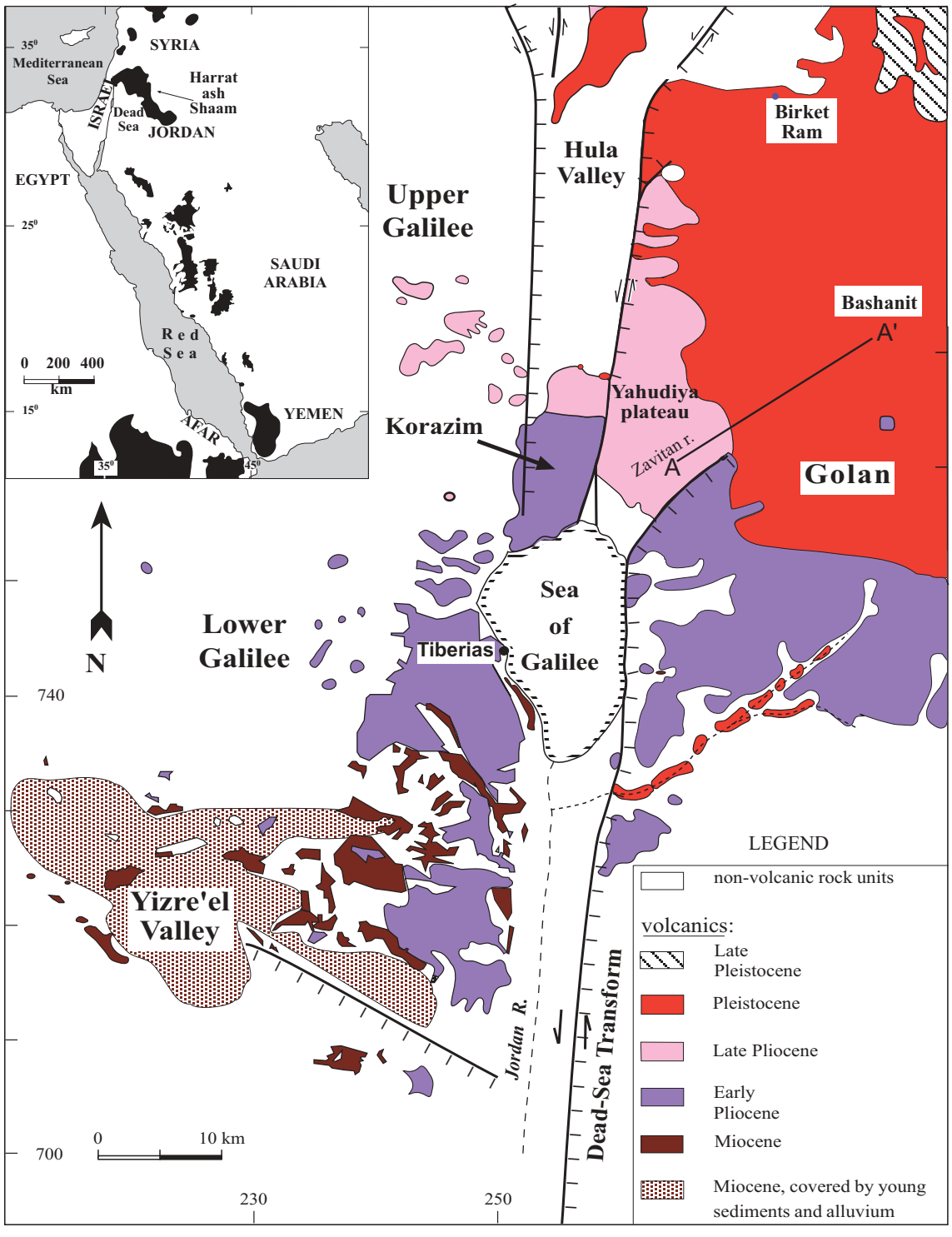

Fig. 1. Map of the volcanism in northern Israel (coordinates are the new Israel grid). The ages of the volcanic rocks are based on K–Ar ages mainly determined by Heimann (1990), Shaliv (1991), Mor (1993), Heimann *et al.* (1996) and during the current study (the central Golan, Table 1). Inset map shows the distribution of Cenozoic magmatism in the western Arabian peninsula.

Table 1: Geochemistry of representative Plio-Pleistocene Golan–Galilee basalts

Sample:	Wy-165	Wy-228	Wy-136	Wy-147	Wy-308	Wy-309	UK-4126	Wy-337	Wy-128
Region:	Galilee-S	Galilee-S	Galilee-S	Galilee-S	Galilee-N	Galilee-S	Galilee-S	Golan-S	Golan-S
Location:	1964/2196	1993/2223	1978/2448	1976/2447	1944/2704	1945/2704	1959/2571	2130/2407	
Age:	E. Plio.	E. Plio.	E. Plio.	E. Plio.	L. Plio.	L. Plio.	L. Plio.	E. Plio.	E. Plio.
K–Ar age:*		5·2 Ma							
Rock type:†	alk. bas.	alk. bas.	alk. bas.	hawaiite	basanite	basanite	basanite	alk. bas.	alk. bas.
Phenocr.:‡	ol	*ol* cpx plg	ol	ol	ol	ol	ol cpx	ol	ol *plg*
wt %									
SiO_2	44·0	48·3	48·3	45·7	43·8	43·6	43·5	47·8	47·7
TiO_2	2·43	2·47	1·87	2·86	3·25	3·27	3·10	2·14	2·25
Al_2O_3	13·53	15·34	14·97	15·39	13·78	13·88	13·84	15·31	15·68
Fe_2O_3	1·27	1·29	1·29	1·18	1·28	1·28	1·25	1·30	1·26
FeO	10·28	10·48	10·45	9·52	10·33	10·33	10·08	10·55	10·17
MnO	0·17	0·16	0·16	0·16	0·17	0·17	0·16	0·17	0·16
MgO	10·00	5·78	7·94	7·88	7·00	7·15	6·83	6·55	6·47
CaO	9·80	9·40	9·06	8·63	9·52	9·83	10·49	9·83	9·97
Na_2O	2·64	3·38	3·21	3·53	5·09	4·67	5·13	3·31	3·37
K_2O	1·27	0·87	0·70	2·00	0·97	0·88	1·05	0·75	0·82
P_2O_5	0·49	0·29	0·16	0·59	1·37	1·37	1·42	0·22	0·29
LOI	2·95	1·77	1·42	2·03	2·77	3·23	2·64	1·98	1·80
Total	98·79	99·52	99·55	99·43	99·32	99·63	99·50	99·90	99·89
Mg-no.	0·63	0·50	0·58	0·60	0·55	0·55	0·55	0·53	0·53
ppm									
V	203	205	181	186	201	189	206	188	219
Cr	211	115	286	144	184	187	165	290	168
Co	57	35	47	46	40	68	42	47	42
Ni	209	51	195	142	154	165	141	112	65
Cu	48	24	50	38	31	32	35	46	43
Zn	98	103	101	97	136	135	129	104	101
Ga	20·5	24·9	22·5	23·8	23	21·6	22·0	22·3	23·4
Rb	14	12	10	26	16	11	6	10	8
Sr	855	562	388	808	1525	1589	1742	441	509
Y	23	20	17	23	26	27	28	19	23
Zr	186	200	128	265	340	344	316	146	164
Nb	37	38	19	55	96	97	95	21	25
Ba	205	174	121	362	627	884	862	159	239
Sc	23·86	24·82							
Cs	0·31	0·26							
La	26·3	15·2	9·5	28·7	53·6	53·1	71·6	10·2	13·9
Ce	53·6	34·5	23·1	65·7	121·4	119·6	151·9	26·6	34·4
Pr			2·9	7·5	14·6	14·5	16·4	3·1	4·3
Nd	28·1	21·2	13·5	33·5	63·9	64·2	73·4	15·7	20·3
Sm	6·14	4·79	3·22	6·58	11·56	11·68	12·34	3·70	4·46
Eu	2·2	1·86	1·22	2·04	3·43	3·43	3·76	1·34	1·53
Gd	6·14		2·80	5·14	8·56	8·61	9·16	3·38	3·85
Tb	0·97	0·79	0·47	0·74	1·06	1·06	1·15	0·51	0·59
Dy			2·78	4·09	5·37	5·40	5·23	3·12	3·51
Ho	0·84	0·91	0·51	0·69	0·86	0·86	0·81	0·57	0·64
Er			1·36	1·78	2·08	2·05	1·99	1·52	1·73
Tm			0·21	0·22	0·24	0·23	0·24	0·20	0·23
Yb	1·58	1·59	1·18	1·35	1·51	1·52	1·38	1·33	1·49
Lu	0·22	0·20	0·21	0·19	0·19	0·19	0·18	0·19	0·22
Hf	4·30	4·64	3·10	5·99	6·49	6·17	5·28	3·47	3·87
Ta	2·20	2·34	1·68	5·09	2·37	2·41	4·86	1·78	2·54
Pb			1·08	2·41	3·32	2·92	3·71	1·14	1·22
Th	2·66	1·91	1·83	4·16	5·49	5·51	7·35	1·11	1·57
U	0·91	0·45	0·28	0·84	1·37	1·37	1·55	0·17	0·34
$^{143}Nd/^{144}Nd$			0·512908			0·512872		0·512883	
$^{87}Sr/^{86}Sr$								0·703371	
$^{87}Sr/^{86}Sr$ (6N)								0·703315	

Table 1: continued

Sample:	Wy-254	Wy-257	Wy-292	Wy-290	Wy-287	Wy-282	Wy-280	Wy-279	Wy-278
Region:	S. Golan	S. Golan	W. Golan	W. Golan	W. Golan	W. Golan	W. Golan	W. Golan	W. Golan
Location:	2182/2558	2182/2556	2143/2612	2144/2613	2144/2612	2143/2614	2143/2614	2143/2614	2143/2614
Age:	E. Plio.	E. Plio.	E. Plio.	L. Plio.	L. Plio.	L. Plio.	L. Plio.	L. Plio.	L. Plio.
K–Ar age:*	4·4 Ma		*3·3 Ma*	*3·0 Ma*			*2·3 Ma*		
Rock type:†	alk. bas.	hawaiite	basanite	alk. bas.	alk. bas.	alk. bas.	alk. bas.	alk. bas.	alk. bas.
Phenocr.:‡	ol	*ol* cpx	ol	ol	ol	ol	*ol* cpx	*ol* cpx	ol
wt %									
SiO_2	47·9	47·0	43·0	47·7	46·3	46·8	47·4	48·1	46·0
TiO_2	2·04	2·39	2·63	2·32	2·23	2·06	2·48	2·39	2·49
Al_2O_3	13·98	15·06	13·03	14·33	14·49	14·98	14·33	16·39	14·27
Fe_2O_3	1·30	1·27	1·36	1·28	1·32	1·32	1·26	1·12	1·34
FeO	10·49	10·29	11·03	10·37	10·71	10·70	10·22	9·08	10·87
MnO	0·16	0·17	0·19	0·16	0·16	0·17	0·17	0·14	0·17
MgO	9·07	7·54	10·54	8·24	9·03	9·01	8·34	6·30	8·60
CaO	8·90	8·58	10·72	9·03	9·67	9·41	9·00	10·49	9·46
Na_2O	3·13	3·71	3·06	3·14	3·20	3·06	3·35	3·00	3·58
K_2O	0·89	1·51	1·25	1·04	0·92	0·76	1·16	1·12	1·15
P_2O_5	0·29	0·41	1·18	0·44	0·55	0·38	0·52	0·33	0·64
LOI	2·45	1·95	2·00	2·31	1·51	1·65	1·55	1·46	1·02
Total	100·57	99·87	99·97	100·34	100·11	100·25	99·82	99·94	99·61
Mg-no.	0·61	0·57	0·63	0·59	0·60	0·60	0·59	0·55	0·59
ppm									
V	187	185	193	181	184	199	190	218	189
Cr	325	201	301	218	268	267	253	147	201
Co	46	44	54	47	57	58	53	37	59
Ni	240	159	259	159	226	234	170	100	198
Cu	48	42	48	41	44	49	39	40	47
Zn	110	105	122	112	115	107	113	96	118
Ga	20·7	21·9	21·1	21·9	20·4	20·5	20·5	23	21·4
Rb	11	18	23	13	13	11	17	18	16
Sr	509	634	1106	697	852	553	703	782	995
Y	21	22	28	23	20	21	22	21	22
Zr	161	228	276	193	161	129	187	193	199
Nb	26	37	73	34	34	24	38	40	46
Ba	173	196	446	244	290	174	293	256	392
Sc									
Cs									
La	16·5	24·1	44·3	25·0	27·5	19·2	25·5	21·1	35·8
Ce	39·8	54·8	104·6	57·2	64·5	45·5	59·5	49·7	78·0
Pr	4·8	5·7	12·4	6·3	7·1	5·1	7·1	6·0	8·5
Nd	22·0	26·2	54·6	30·3	33·3	24·2	31·5	27·0	39·3
Sm	4·71	5·26	10·10	6·02	6·31	5·20	6·07	5·67	7·40
Eu	1·45	1·89	3·12	2·08	2·17	1·85	2·01	1·80	2·67
Gd	3·79	4·35	8·27	5·05	4·93	4·09	4·89	4·43	5·66
Tb	0·54	0·63	1·07	0·76	0·72	0·77	0·69	0·63	0·91
Dy	3·32	3·48	5·63	3·87	3·54	3·45	3·99	3·70	3·72
Ho	0·60	0·54	0·98	0·66	0·59	0·66	0·68	0·65	0·62
Er	1·57	1·53	2·31	1·76	1·51	1·60	1·72	1·72	1·53
Tm	0·21	0·15	0·28	0·23	0·19	0·26	0·21	0·21	0·21
Yb	1·27	1·30	1·72	1·48	1·23	1·44	1·45	1·4	1·22
Lu	0·20	0·14	0·23	0·19	0·17	0·23	0·19	0·19	0·18
Hf	3·94	3·95	5·72	3·66	2·80	2·66	4·26	4·60	3·53
Ta	2·31	3·67	4·19	2·29	1·09	1·57	2·48	3·25	1·27
Pb	1·66	2·25	2·34	1·74	1·64	1·11	2·03	2·01	2·15
Th	2·40	3·07	3·76	2·91	2·62	2·04	3·15	2·90	3·54
U	0·55	0·74	0·95	0·57	0·46	0·40	0·74	0·60	0·67
$^{143}Nd/^{144}Nd$		0·512897	0·512901		0·512861	0·512848		0·512875	0·512866
$^{87}Sr/^{86}Sr$		0·703212	0·703116		0·703199	0·703246		0·703290	0·703191
$^{87}Sr/^{86}Sr$ (6N)					0·703160	0·703181			0·703181

Table 1: continued

Sample:	Wy-276	Wy-8	Wy-235	Wy-242	Wy-239	Wy-18	Wy-29	Wy-52	Wy-232	Wy-16
Region:	W. Golan	Golan	Golan	Golan	Golan	Golan	Golan	Golan	Golan	Golan
Location:	2143/2615	2213/2775	2188/2668	2233/2664	2246/2667	2226/2810	2235/2787	2241/2794	2299/2729	2299/2729
Age:	L. Plio.	E. Pleist.	E. Pleist.	E. Pleist.	L. Pleist.	L. Pleist.	L. Pleist.	L. Pleist.	L. Pleist.	L. Pleist.
K–Ar age:*	*1·8 Ma*	0·8 Ma	*0·7 Ma*	*0·9 Ma*					*0·44 Ma*	
Rock type:†	alk. bas.	basanite	alk. bas.	hawaiite	hawaiite	basanite	basanite	basanite	basanite	basanite
Phenocr.:‡	ol	ol cpx	ol	*ol* cpx	ol cpx	*ol* cpx	*ol* cpx	*ol* cpx	ol *cpx*	ol *cpx*
wt %										
SiO_2	46·0	44·6	45·5	45·0	45·7	43·8	44·8	43·6	45·5	44·0
TiO_2	2·40	2·89	2·71	2·78	2·68	2·73	2·60	2·61	2·99	2·52
Al_2O_3	14·17	15·50	13·64	13·88	13·94	13·88	14·00	14·70	15·13	14·20
Fe_2O_3	1·36	1·24	1·29	1·30	1·26	1·17	1·28	1·20	1·20	1·14
FeO	10·98	10·04	10·41	10·56	10·23	9·48	10·37	9·72	9·69	9·23
MnO	0·17	0·14	0·16	0·16	0·16	0·16	0·14	0·18	0·16	0·14
MgO	8·76	6·10	8·76	8·23	8·33	8·27	9·10	8·80	5·96	8·40
CaO	9·47	10·20	9·49	9·76	9·62	10·27	10·40	10·20	10·65	10·30
Na_2O	3·61	4·19	3·57	3·65	3·99	4·43	4·10	3·09	3·93	4·54
K_2O	1·01	1·77	1·29	1·36	1·39	1·88	1·57	1·41	1·62	1·82
P_2O_5	0·57	1·40	0·87	1·02	1·00	1·74	1·30	1·90	0·98	2·00
LOI	1·24	1·28	1·92	1·70	1·52	1·23	1·26	2·23	1·84	0·76
Total	99·69	99·35	99·59	99·40	99·77	99·08	100·92	99·64	99·60	99·05
Mg-no.	0·59	0·52	0·60	0·58	0·59	0·61	0·61	0·62	0·52	0·62
ppm										
V	185	194	190	176	177	190	203	161	229	183
Cr	213	98	210	190	161	159	222	167	79	183
Co	51	36	51	46	49	43	49	51	38	46
Ni	200	71	195	193	174	144	192	158	56	141
Cu	45	49	44	40	44	35	51	39	49	48
Zn	116	108	124	122	130	130	113	130	121	125
Ga	22·2	24·1	20·6	21·4	21·6	21·3	19·6	21·2	23·7	21·0
Rb	13	24	13	13	16	26	14	16	20	25
Sr	845	1457	1695	1723	1435	1809	1408	1789	1457	1741
Y	23	30	24	25	26	27	27	28	26	28
Zr	173	267	236	244	253	317	208	322	287	293
Nb	38	81	55	57	65	96	55	98	90	93
Ba	321	715	558	729	589	849	578	824	603	780
Sc		17·32					20·73	19·31		18·34
Cs		0·42					0·17	0·43		0·28
La	29·9	61·7	44·0	57·0	48·2	80·4	55·5	95·4	58·3	92·6
Ce	68·0	116·1	99·7	121·0	109·9	153·3	110·9	168·7	123·3	160·2
Pr	7·9	15·5	12·1	13·5	13·1	17·5		19·1	13·4	
Nd	36·1	57·0	52·4	61·1	57·6	66·6	57·7	77·0	60·2	75·9
Sm	6·59	10·53	8·95	10·15	10·26	13·89	10·35	12·74	10·34	12·54
Eu	2·17	3·52	2·73	3·27	3·00	3·99	3·54	4·30	3·19	4·08
Gd	5·35	9·13	6·45	7·57	7·61	13·38	9·80	11·56	7·50	9·4
Tb	0·75	1·37	0·81	0·89	0·92	1·24	1·43	1·55	0·99	1·47
Dy	4·03		4·37	4·44	4·85	5·93			4·61	
Ho	0·69	1·07	0·69	0·62	0·81	0·98	0·98	1·19	0·75	1·16
Er	1·82		1·77	1·73	2·00	2·32			1·92	
Tm	0·22		0·22	0·15	0·26	0·28			0·23	0·33
Yb	1·48	1·77	1·31	1·22	1·55	1·64	1·61	1·65	1·40	1·61
Lu	0·19	0·21	0·19	0·13	0·21	0·23	0·21	0·23	0·19	0·20
Hf	4·37	5·47	5·02	3·92	3·14	5·14	4·86	6·08	4·43	5·64
Ta	2·99	3·91	1·91	1·15	1·39		3·33	4·77	1·18	4·49
Pb	2·11	3·87	2·78	2·70	3·36	5·40		4·43	3·00	
Th	3·13	5·17	3·32	3·41	3·97	8·29	4·09	8·82	6·24	8·43
U	0·66	1·40	0·76	0·80	0·95	2·07	0·99	2·28	1·25	2·04
$^{143}Nd/^{144}Nd$				0·512859	0·512854	0·512864	0·512844	0·512888		
$^{87}Sr/^{86}Sr$				0·703150		0·703168		0·703142		
$^{87}Sr/^{86}Sr$ (6N)				0·703119		0·703151		0·703140		

*K–Ar ages of the specific basaltic flow (for references see Fig. 1). Ages in italics are from this study.
†Rock type defined according to Le Bas *et al.* (1986); alk. bas., alkali basalt.
‡ol, olivine; cpx, clinopyroxene; plg, plagioclase. Mineral in italics is the dominant phenocryst phase.
LOI is reported corrected for the amount of iron oxidized during the ignition.
$^{87}Sr/^{86}Sr$ (6N) is the isotopic ratio measured after pre-leaching samples in 6N instead of the usual 0·5N HCl.

(Heimann, 1990; Heimann *et al.*, 1996; Hurwitz *et al.*, 2002), whereas Late Pliocene and Early Pleistocene basalts are found only further north, in northern Korazim and in the subsurface and around the Hula Valley (Fig. 1, Heimann, 1990; Mor, 1993).

The main active tectonic features in the region are the Red Sea rift and the Dead Sea Transform fault (inset to Fig. 1). The Red Sea trends N25W. Rifting started at 26 Ma, accompanied (or pre-dated) by uplift and volcanism on the Arabian side (e.g. Omar & Steckler, 1995; Menzies *et al.*, 1997). Seafloor spreading commenced at about 5 Ma along the southern part of the axial trough. The Dead Sea Transform fault separates the Arabian plate, which includes the Golan, from the Sinai sub-plate including the Yizre'el Valley and the Galilee. The fault trends north–south and the total amount of left-lateral slip along it is about 105 km (Quennell, 1958; Freund *et al.*, 1970; Freund, 1978; Garfunkel *et al.*, 1981). It is commonly accepted that this displacement has accumulated during the past 20 Myr (Bartov *et al.*, 1980) and that an offset of 60 km had already occurred by the end of the Miocene (5 Ma), before the Early Pliocene volcanism started (Freund, 1978; Garfunkel *et al.*, 1981). A series of pull-apart basins (e.g. the Dead Sea, the Sea of Galilee and the Hula Valley, Fig. 1) was developed along the Dead Sea Transform as a result of sideways stepping of the major fault planes (see Garfunkel, 1981; Garfunkel & Ben Avraham, 2001). Pliocene and Plio-Pleistocene basalts are buried in the Sea of Galilee and the Hula Valley basins, respectively, under hundreds to thousands of meters of fluvio-lacustrine sediments.

SAMPLING AND ANALYTICAL METHODS

Ninety-seven samples were collected from volcanic outcrops in the Golan and the Galilee, representing the entire Plio-Pleistocene sequence on both sides of the Dead Sea Transform. About 100 g of fresh rock pieces were crushed and ground to fine powder (<200 mesh) for chemical and isotopic analyses, and thin sections were prepared for petrographic studies.

Concentrations of major elements were determined by X-ray fluorescence (XRF) using a wavelength Philips PW-1404 system at Guttenberg University, Mainz, using glass discs. Calibration curves were established using international standards [recommended values from Govindaraju (1989) and Jochum *et al.* (1990)]. Fe was determined as $Fe_2O_{3(total)}$; Fe^{2+} was assumed to be 90% of the total iron. Accuracy was within 1–2% for most elements (accuracies of Na and Mn are 4% and 5%, respectively). Reproducibility was measured by running duplicates within run and in separate runs and was found to be better than 2% for most elements and 4% for Na. In 12 samples, concentrations of major elements were determined by inductively coupled plasma atomic emission spectrometry (ICP-AES; Weinstein *et al.*, 1994), and three of these samples were remeasured by XRF. The two methods agree within a few per cent for most of the elements, except for P concentrations, which were consistently higher (by 6–9%) in the ICP-AES measurements. For these three samples, we use the XRF data. Loss on ignition (LOI) was determined by heating 1 g of a sample to about 1100°C, and was corrected for oxidation of ferrous iron during heating. Calculated LOI values are considered as maximum values, as many basalts are relatively oxidized.

Concentrations of trace elements (V, Cr, Co, Ni, Cu, Zn, Ga, Rb, Sr, Y, Zr, Nb, Ba) were also determined by XRF using powder pellets. Accuracy is usually better than 10%relative. Ba concentrations measured on one of the standards (BHVO-1) were very different from the recommended values (86 and 139 ppm, respectively), whereas six other standards yielded accuracies better than 10%. This suggests that Ba data should be treated cautiously. Precision of trace elements was also better than 10% relative, except for Ba, for which precision was 16%.

Concentrations of Sc, Cs, Hf, Ta, Pb, Th, U and 14 rare earth elements (REE) in 40 samples were determined by inductively coupled plasma mass spectrometry (ICP-MS) using a VG Plasma Quad II+ system (University of Göttingen) with a peak jump mode [following the procedure described by Gao *et al.* (1999)]. Blanks are negligible for most of the elements, except for Gd and Dy (in some of the runs), which are, therefore, not used below for quantitative modeling. Accuracies are better than 10% for most REE and U (for Tb and Tm accuracy is 20%), whereas those for Ta and Hf are 15% (low stability of HFSE in the solution) and those for Pb and Th are 25% and 30%, respectively (a strong memory effect for Th). Therefore, both the Pb and Th data should be interpreted cautiously. Sc was consistently higher (by about 20%) than the recommended values for international standards as a result of interference with HCO_2. Cs was lower by 20%. Therefore, both Sc and Cs measured by ICP-MS are not reported in this study.

The concentrations of Sc, Cs, Hf, Ta, Th, U and 11 REE in 15 samples were determined by instrumental neutron activation analysis (INAA) in the University of Karlsruhe, following the procedure described by Kramar & Puchelt (1982). Accuracies are between 0 and 15%. Comparative analyses of six samples (three of them from the current study) show that there is a good agreement between INAA and ICP-MS measurements for La, Ce, Nd, Sm, Eu, Gd, Yb, Lu, Th and U (<20% difference), whereas Tb, Ho, Ta and Hf are in significant disagreement [for the last two this is probably because

of the problem of high field strength element (HFSE) stabilization in solutions during ICP-MS analyses]. For the three comparative samples, the reported data (Table 1) are those from the INAA (except for the Pb and Pr data, which are from the ICP-MS measurements).

Rock powder (100 mg) was leached for about 40 min in warm 0·5N HCl to remove secondary Sr. Leaching experiments on some of the samples showed that the main difference in the Sr isotope ratios of the treated basalts is between no leaching and 0·5N HCl, whereas the effect of changing to stronger acid (e.g. 6N HCl, Table 1) was within the analytical error of the laboratory (an average difference of $2{\cdot}3 \times 10^{-5}$). After washing and drying, the samples were digested by 3 ml of 24N HF + 0·5 ml of 14N HNO_3 for at least 8 h at 120°C, and evaporated at 140°C (some of the samples were heated for an additional 2 h at 180°C to break the fluorides). The evaporates were then dissolved in diluted HNO_3 (120°C), checked for complete dissolution, evaporated and redissolved by 6N HCl (70–80°C). After evaporation to dryness, the residue was taken up by 3·2 ml of 2·6N HCl and centrifuged in Teflon tubes. Solutions (2 ml) were loaded on columns consisting of ~15 ml cation exchange (preconditioned by 20 ml of 2·6N HCl). The columns were then washed by additional 42 ml of 2·6N HCl (eluting most of the elements except for Sr and the REE), and then most of the Sr was eluted from the column by another 6 ml of 2·6N HCl. After 10 ml wash (14 ml in the last few samples) by 6N HCl, the REE were eluted by an additional 6 ml of 6N HCl. After drying, both Sr and REE aliquots were treated with HNO_3 to destroy residual resin and dried again. REE aliquots were taken by 0·5 ml of 0·18N HCl and loaded on columns consisting of 0·5 g orthophosphoric acid (1·5N) mixed with 5 g Teflon beads (after conditioning the columns with 0·18N HCl). The columns were washed with an additional 7·5 ml of 0·18N HCl, and the Nd was eluted with an additional 6 ml and dried. All chemical procedures were carried out in a clean environment, and all the acids used were double distilled. Blanks were negligible. Isotopic analyses were carried out on a Finnigan MAT 262 mass spectrometer at the Geochemistry Institute, University of Göttingen, equipped with nine Faraday cups and using a multicollector static mode for all elements. For Sr isotope analysis, about 4 ng were loaded with phosphoric acid onto Ta single filaments (except for the standard NBS-987, which was loaded onto Re filaments). Sr analyses were corrected for mass fractionation by normalizing to $^{88}Sr/^{86}Sr = 8{\cdot}375209$. The NBS-987 standard was routinely measured, giving a mean $^{87}Sr/^{86}Sr$ value of 0·710229 and a reproducibility (2σ) of 18×10^{-6} ($n = 13$). The mean of all NBS-987 measured in the laboratory during the period September 1995 to July 1996 was 0·710244 ($2\sigma = 32 \times 10^{-6}$). For Nd isotope analysis, about 1 ng was loaded onto Re double filaments. Isotope ratios were normalized to $^{146}Nd/^{144}Nd = 0{\cdot}7219$. The measured mean $^{143}Nd/^{144}Nd$ for the La Jolla Nd standard was 0·511848 with a reproducibility of 16×10^{-6} (2σ, $n = 11$), whereas the mean for the period September 1995 to July 1996 was 0·511851 ($2\sigma = 18 \times 10^{-6}$). All isotopic ratios measured (Sr, Nd) are considered as initial ratios because of the relatively young ages (0–5 Ma) of the basalts studied and their relatively low Rb/Sr ratios.

K–Ar ages were determined by A. Heimann (Geological Survey of Israel). Details of the analytical procedures have been given by Heimann *et al.* (1996).

PETROGRAPHY AND CHEMISTRY OF THE GOLAN–GALILEE BASALTS

General description and petrography of the Golan–Galilee basalts

The volcanic rocks of the Galilee and the Golan are mainly composed of basaltic flows. Scoriaceous rocks are mostly restricted to the young cinder cones of the northern Golan (Pleistocene) and of the Upper Galilee (Late Pliocene), although a few scoria exposures are also found amongst the Early Pliocene rocks of the southern Golan. Tuff deposits are very rare, and are not included in this study.

We subdivide the Plio-Pleistocene Golan–Galilee volcanism into six units according to age and location (Fig. 1). These are, in order: Early Pliocene basalts from the southeastern (Lower) Galilee, Late Pliocene basalts from the northeastern (Upper) Galilee, Early Pliocene basalts from the southern Golan, Late Pliocene basalts from the western Golan, Early Pleistocene basalts from the eastern and northern Golan, and Late Pleistocene basalts and scoria also from the eastern and northern Golan. In most figures, we refer to both Golan Pleistocene units as one group.

Most Golan–Galilee samples typically show porphyritic to glomeroporphyritic textures, with the phenocrysts usually dominated by olivine (Fo78 to Fo85, 5–20% of the rock; Table 1), which is often partly or completely replaced by iddingsite. Clinopyroxene phenocrysts occur in smaller proportions (<5%), and they are rare in the Early and Late Pliocene basalts. Early Pleistocene basalts from the Golan are the only group that shows similar proportions of olivine and clinopyroxene phenocrysts (2–3%). Plagioclase phenocrysts (labradorite, usually <1%) are observed in about 20% of the samples, mainly those of Early Pliocene age. The groundmass of all Early Pliocene and of Golan Late Pliocene basalts is mostly medium grained, whereas that of Galilee Late Pliocene and of Golan Pleistocene basalts is usually fine grained, with a pilotaxitic texture dominated by plagioclase laths and prismatic crystals of clinopyroxene. Intergranular

nepheline is also common. The groundmass of the scoriaceous rocks usually shows a hyalopilitic texture, although the glass is usually replaced. Calcite amygdules are common in the Pliocene basalts.

Mantle xenoliths are common in the Golan and Galilee basalts, though usually restricted to the basanitic units. Spinel peridotites are found both in the Golan Late Pleistocene and in the Upper Galilee Late Pliocene basanites. Pyroxenites are found just in one Pleistocene maar from the northern Golan (Birket Ram, Fig. 1). The xenolith assemblage of this maar is especially large and variable, containing peridotites, dry and hydrous pyroxenites, mafic granulites and megacrysts of kaersutite and microcline (Mittlefehldt, 1984; Stein, 1987). Mafic granulites (as well as anorthoclase megacrysts) were also found in an Early Pliocene Lower Galilee site (Gazit, 2005).

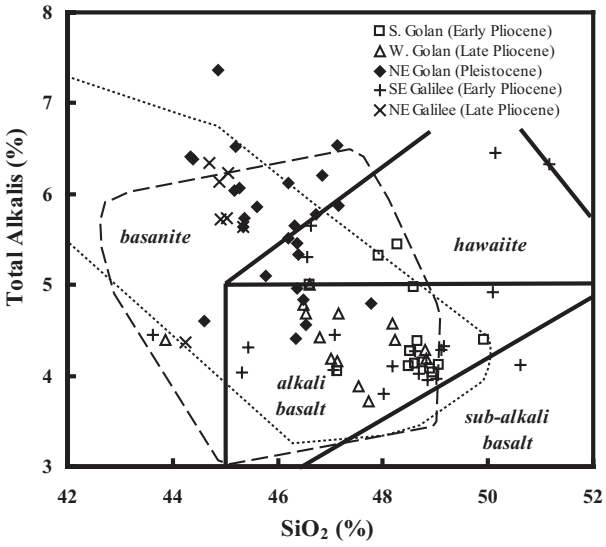

Fig. 2. TAS (total alkalis vs SiO_2; Le Bas *et al.*, 1986) diagram showing the classification of the Golan and Galilee Plio-Pleistocene basalts. Also shown are fields for Middle Miocene basalts from the Yizre'el Valley and southeastern Galilee (Weinstein, 2000; excluding two nephelinites with 38 and 40% SiO_2; dashed line) and Miocene to Pleistocene basalts from northeastern Jordan (Shaw *et al.*, 2003; dotted line). All data are plotted on a volatile-free basis.

Major and trace element geochemistry of the basalts

The bulk-rock major and trace element compositions of representative Golan–Galilee basalts are given in Table 1. The complete dataset is available for downloading from the *Journal of Petrology* website at http://www.petrology.oupjournals.org. The samples mainly plot in the basanite, hawaiite and alkali basalt fields of the total alkalis vs silica (TAS) diagram (Fig. 2), and show a trend of increasing total alkali concentration ($Na_2O + K_2O$) with decreasing silica. SiO_2 concentrations range between 43% and 51% and total alkalis between 3·5% and 7·5%. The spectrum of compositions (alkali basalt–hawaiite–basanite) is similar to that of the Neogene–Quaternary basalts from northeastern Jordan (another part of the Harrat ash Shaam volcanic field; Shaw *et al.*, 2003), although the Golan–Galilee basalts are slightly higher in SiO_2 (Fig. 2). Miocene basalts from the Yizre'el Valley and the southeastern Galilee (Fig. 1) are somewhat different. These extend to lower SiO_2 concentrations than the Plio-Pleistocene basalts (including nephelinites with 38–40% SiO_2, not shown in Fig. 2; Weinstein, 2000) but show no systematic increase of alkalis with decreasing SiO_2 (Fig. 2).

Most Golan–Galilee samples have MgO >7% (up to 11·6%) and Mg numbers from 0·55 to 0·66 (Fig. 3a). The hawaiites typically have lower MgO concentrations, implying a relatively higher degree of differentiation. Alumina (12–15% Al_2O_3), and to a lesser extent Na_2O (2·6–5·1%), correlate negatively with MgO (Fig. 3b and c). All other major elements (e.g. CaO, Fig. 3d) do not show any correlation with MgO (either general or within-suite). Nickel (3–326 ppm), Cr (5–423 ppm) and, to a lesser extent, Co (22–68 ppm) correlate positively with MgO concentration (Fig. 3g and h), reflecting olivine and clinopyroxene fractionation. On the other hand, incompatible elements, as well as TiO_2 and P_2O_5, do not correlate with MgO (Figs 3e, f and 4a–d), implying that the variability in their concentrations is not controlled by fractional crystallization. However, they correlate positively with each other and negatively with SiO_2 (Fig. 4e–h).

Primitive mantle normalized incompatible trace element patterns (Fig. 5a–c) are similar to those of ocean island basalts (OIB, Fig. 5c), with strong enrichment in most highly incompatible elements. This enrichment is stronger in the basanites than in the alkali basalts. The REE show a continuous decrease of normalized concentrations from La to Yb (Fig. 6; except for a slight positive Eu anomaly in some of the samples), with $(La/Yb)_{CN}$ ratios of 5–20 in the alkali basalts and 18–40 in the basanites (CN indicates chondrite normalized). Concentrations of heavy REE (HREE) in all Golan–Galilee basalts are lower than in typical mid-ocean ridge basalt (MORB) and OIB. Slopes of middle REE (MREE) to HREE are similar to those of OIB in the alkali basalts ($Tb/Yb_{(CN)}$ ratios of 1·6–3·4), but higher in the basanites (2·8–4·2). All Golan–Galilee basalts show prominent anomalies in primitive mantle normalized trace element diagrams (Fig. 5). These include positive anomalies in Ba, Nb, Sr, P and Zr, and negative anomalies in Rb. The positive P anomalies and negative Rb anomalies are more prominent in the basanites than in the alkali basalts (Fig. 5a and b), and the Ba and Nb anomalies do not always exist. In addition, the basanites show negative

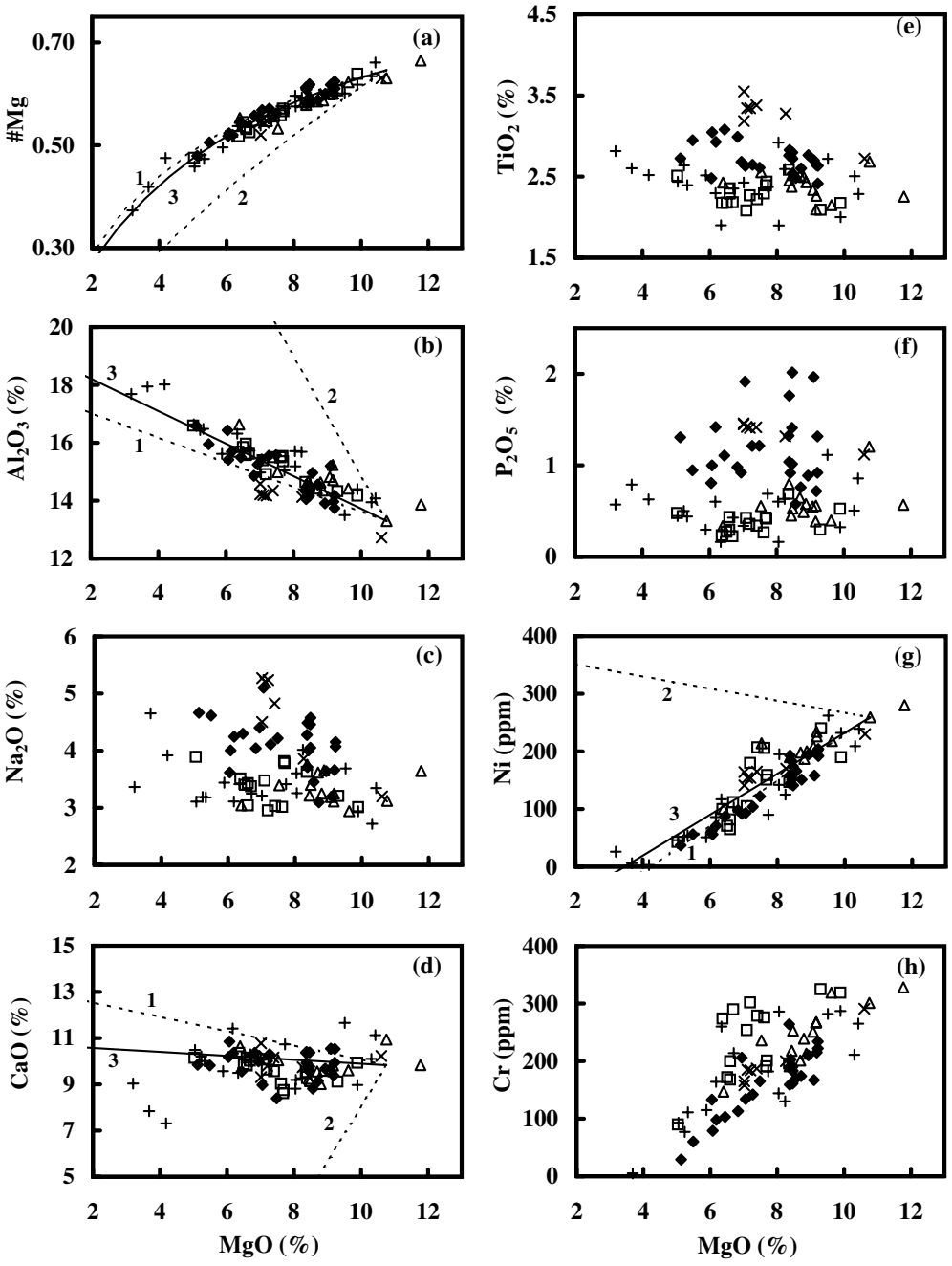

Fig. 3. (a) Mg numbers, (b)–(f) major elements and (g, h) compatible trace elements vs MgO (wt %) in the Golan–Galilee basalts. Symbols are the same as in Fig. 2. Lines show simulations of batch differentiation of (1) olivine, (2) clinopyroxene and (3) a mixture of 60% olivine and 40% clinopyroxene.

anomalies of K and Pb (Fig. 5a and b). In the alkali basalts and in few basanites, there are also negative Th and U anomalies. Basalts from northeastern Jordan show similar Nb, Sr, P, Rb and K anomalies, but they do not show positive Ba and P anomalies (Shaw *et al.*, 2003). In general, the ratios of the REE to their neighboring HFSE in Fig. 5 (e.g. La/Nb, Sm/Zr and Eu/Ti) increase from the alkali basalts to the basanites (Fig. 7a and b). Similarly, P/Zr ratios also increase from alkali basalts to the basanites (Fig. 7c). Basalts from northeastern Jordan show similar trends of increasing La/Nb from alkali basalts to basanites (Fig. 7a; Shaw *et al.*, 2003), although their overall La (and Nb) concentrations are lower than in the Golan–Galilee. On the other hand, in volcanic rocks

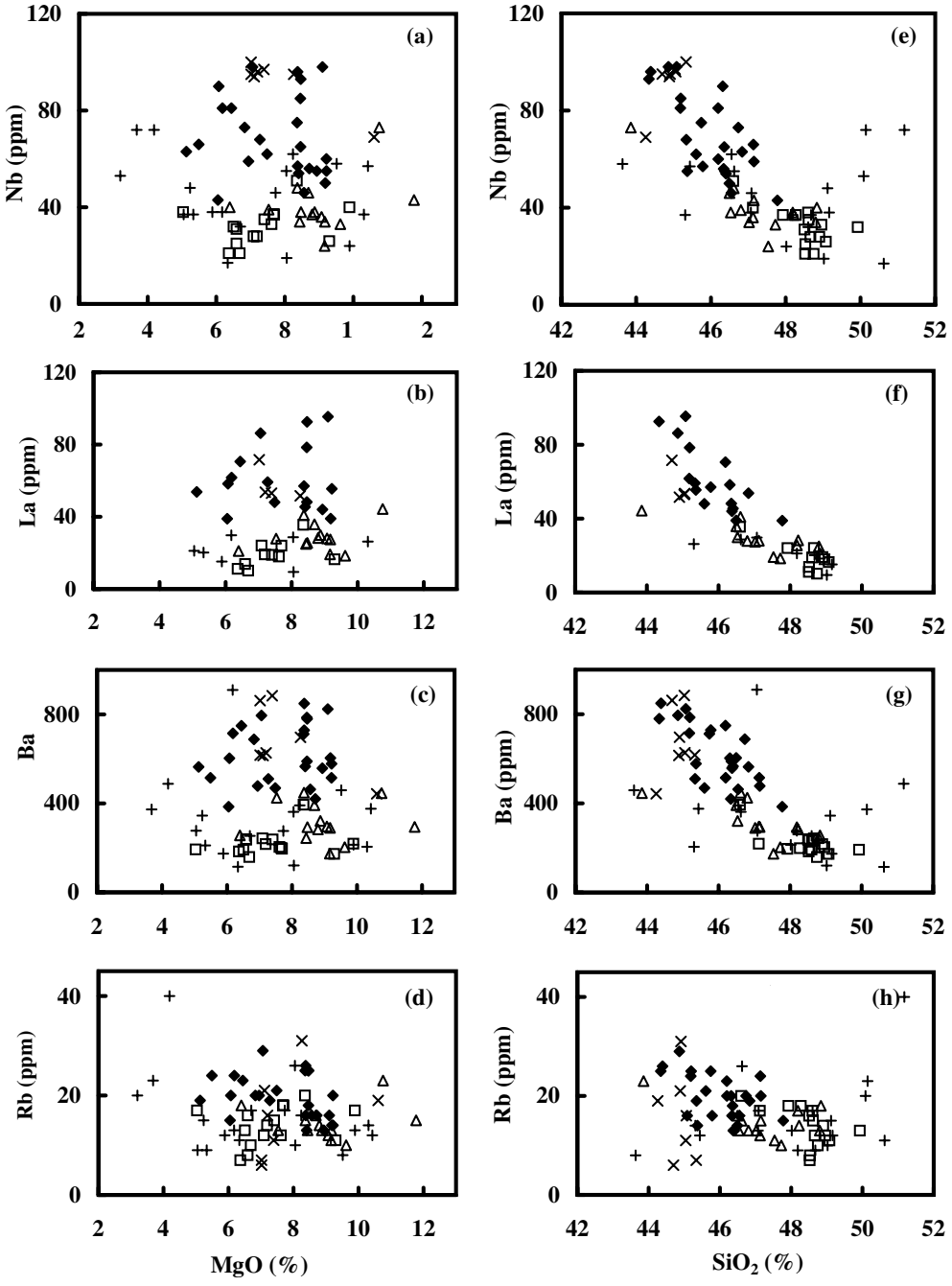

Fig. 4. Concentration of incompatible trace elements vs wt % MgO and wt % SiO_2 in the Golan–Galilee basalts. Symbols are as in Fig. 2.

from the Dead Sea area (Shaw, 2003) La/Nb ratios decrease from alkali basalts to basanites (Fig. 7a).

A central observation in this study is the patterns defined by the Golan–Galilee basalts in plots of some incompatible element ratios vs concentration (e.g. La/Nb vs La, Nb/Zr vs Nb and La/Sm vs La, Fig. 7a–e). In these, the Pliocene alkali basalts define steeper trends than the Pleistocene Golan basanites. The general trends defined by the Golan samples in these diagrams are convex-upward, which we interpret below as mixing curves.

Spatial and temporal variability

In both the Golan and Galilee, basalt chemistry appears to change with both time and geographic location, from alkali basalts in the south to mainly basanites in the north.

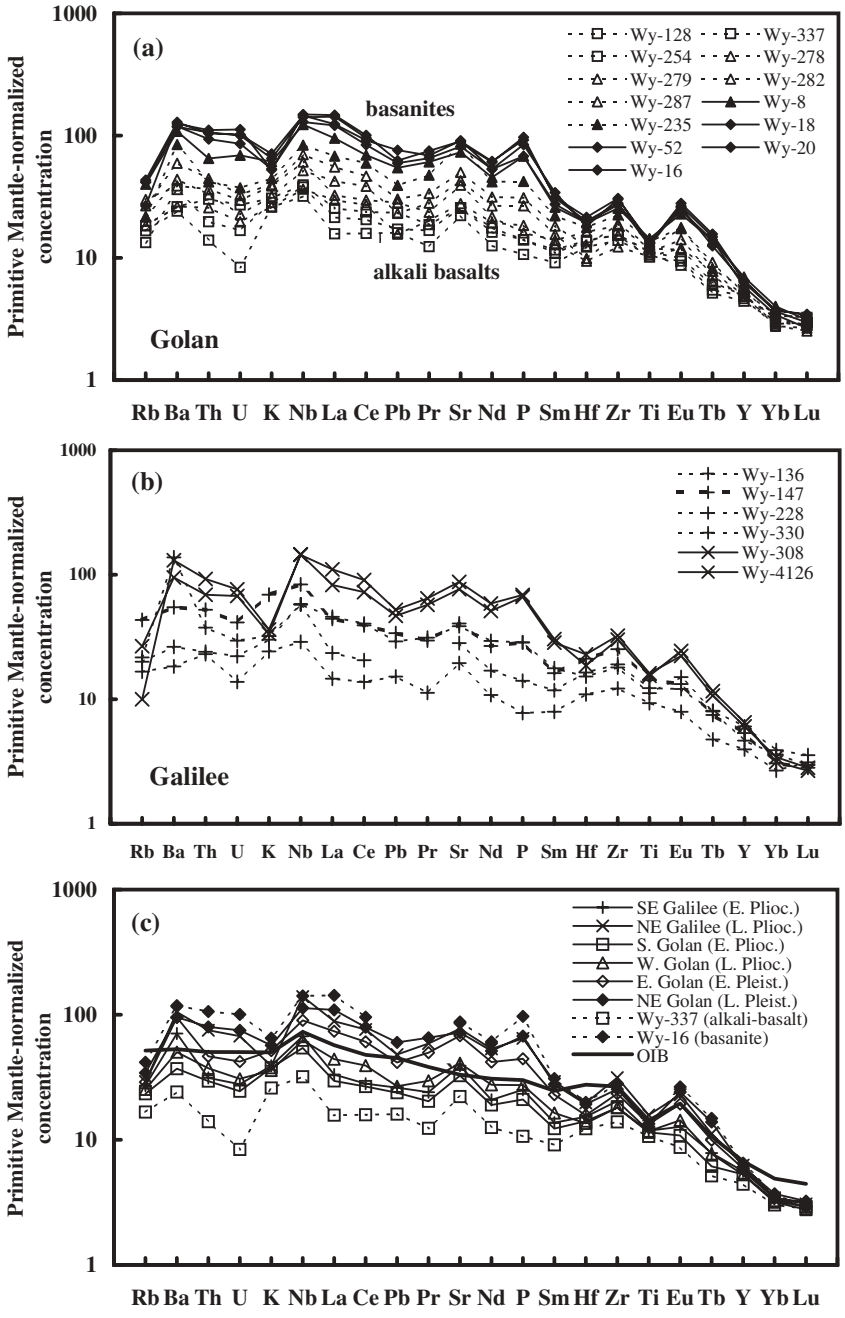

Fig. 5. Primitive mantle normalized trace element diagram showing the composition of representative basalts from (a) Golan, (b) Galilee and (c) averages and end-member compositions (Wy-16 and Wy-337; see text). Symbols are as in Fig. 2, but Pleistocene samples are subdivided into Early (◇) and Late (♦). Dashed lines are for alkali basalts and continuous lines for basanites. Primitive Mantle values are from McDonough & Sun [1995; for Pb, we use the value of 0·071 ppm, recommended by Sun & McDonough (1989)]. The OIB composition is from Sun & McDonough (1989).

In the Golan, Early Pliocene lavas from the south are mainly alkali basalts, with a few hawaiites (Fig. 2). In the western Golan, the Late Pliocene basalts are also alkali basalts, but with lower silica contents (almost all samples contain normative nepheline compared with only 60% of the Early Pliocene samples). Pleistocene lavas from the northern and eastern Golan are mainly basanites and hawaiites (Fig. 2). In the Galilee, Early Pliocene lavas from the south (Lower Galilee) are mainly alkali basalts and hawaiites, whereas Late Pliocene lavas from the north (Upper Galilee) are all basanitic (Fig. 2).

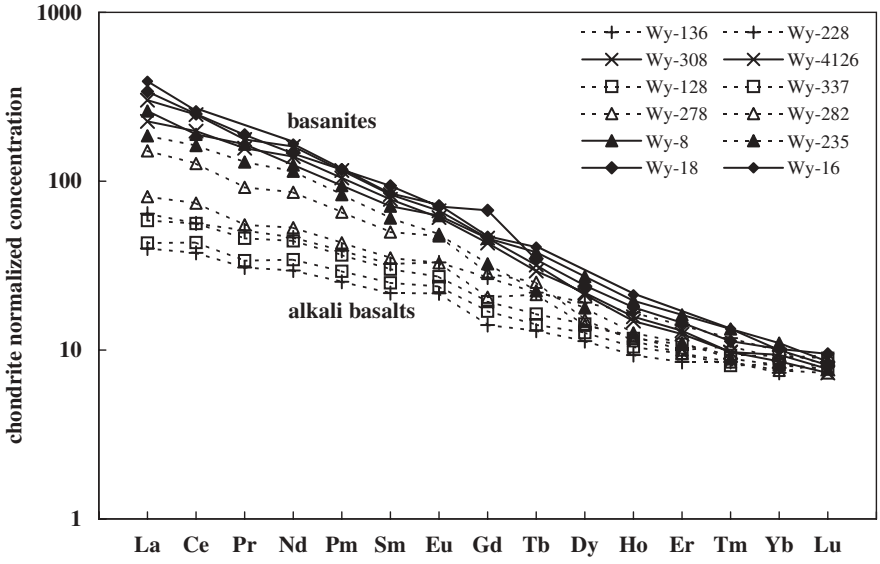

Fig. 6. Chondrite-normalized REE patterns for Golan–Galilee alkali basalts and basanites. Symbols and lines are as in Fig. 5. Chondrite concentrations are from McDonough & Sun (1995).

The spatial–temporal geochemical variability is also reflected in the concentrations of incompatible elements and in H/I ratios (where H indicates a hygromagmatophile, highly incompatible element, and I indicates a moderate incompatible element, e.g. Nb/Zr and La/Sm). Basanites (Golan Pleistocene and Galilee Late Pliocene) have higher incompatible element concentrations and ratios than the alkali basalts (Early Pliocene and most of the Golan Late Pliocene samples; see Figs 5a–c and 7d, e). Also, most of the basanites contain >2·5% TiO_2 and >0·9% P_2O_5 (averages 2·8% and 1·2%, respectively) whereas the alkali basalts have lower concentrations (averages of 2·3% and 0·5%, respectively; Table 1).

Ratios of light REE (LREE) and MREE to HFSE of similar compatibility (e.g. La/Nb, Sm/Zr and Eu/Ti) also increase in the Golan, from the southern Early Pliocene alkali basalts to the northern and eastern Pleistocene basanites (Table 2, Fig. 7a and b). The behavior of P is similar to that of the REE; P/Zr increases from 7–15 in the southern Golan to 15–30 in the northern Golan (Fig. 7c). There is no systematic variability (between suites or within an individual suite) in MgO and compatible element concentrations, except for the Pleistocene basanites from the northern Golan, for which Weinstein *et al.* (1994) observed that Late Pleistocene basalts have higher MgO and Ni concentrations than Early Pleistocene basalts.

An interesting spatial–temporal pattern is shown in the trace element and P concentrations of basalts from the central Golan (Fig. 8). More than half of the samples were taken from flows along a 150 m high cliff section in the Zavitan river in the Yahudiya plateau (western Golan, Fig. 1), spanning a period from the Early to Late Pliocene (3·3–1·8 Ma, Table 1 and Fig. 8). The rest of the samples were collected along a line drawn from the Zavitan river to the Bashanit area in the eastern Golan (A–A' in Fig. 1). The samples along this line are all Pleistocene in age (1·3–0·4 Ma, Table 1 and Fig. 8), but there is no clear trend of decreasing age toward the NE (Fig. 8), even though the easternmost sample is also the youngest. In general, the concentration of P and incompatible elements in the Pleistocene samples is higher than in the Pliocene ones. However, whereas during the Late Pliocene there is a clear temporal trend of increasing concentrations with time, in the Pleistocene samples the main change is with location (towards the NE) and not with time (e.g. concentrations of all three elements increase from the 0·7 Ma sample to the 1·3 Ma one), even though the youngest sample also has the highest concentrations. We note that the location of the vents that fed the Late Pliocene basalts of the Yahudiya plateau is unknown. They could either be further to the east (now covered by Pleistocene basalts, Fig. 1) or unexposed local fissures in the western Golan. Thus, the control on the variation in basalt composition in the central Golan is both temporal and spatial.

Unlike the Golan–Galilee, Neogene–Quaternary basalts from northeastern Jordan do not show any temporal or spatial patterns (Shaw *et al.*, 2003).

Sr and Nd isotope geochemistry

The Sr–Nd isotopic compositions of the Golan–Galilee alkali basalts and basanites are given in Table 1 and plotted in Fig. 9a and b. Nd isotope ratios are remarkably uniform in the range $\varepsilon Nd = 4{\cdot}0–5{\cdot}2$, whereas $^{87}Sr/^{86}Sr$

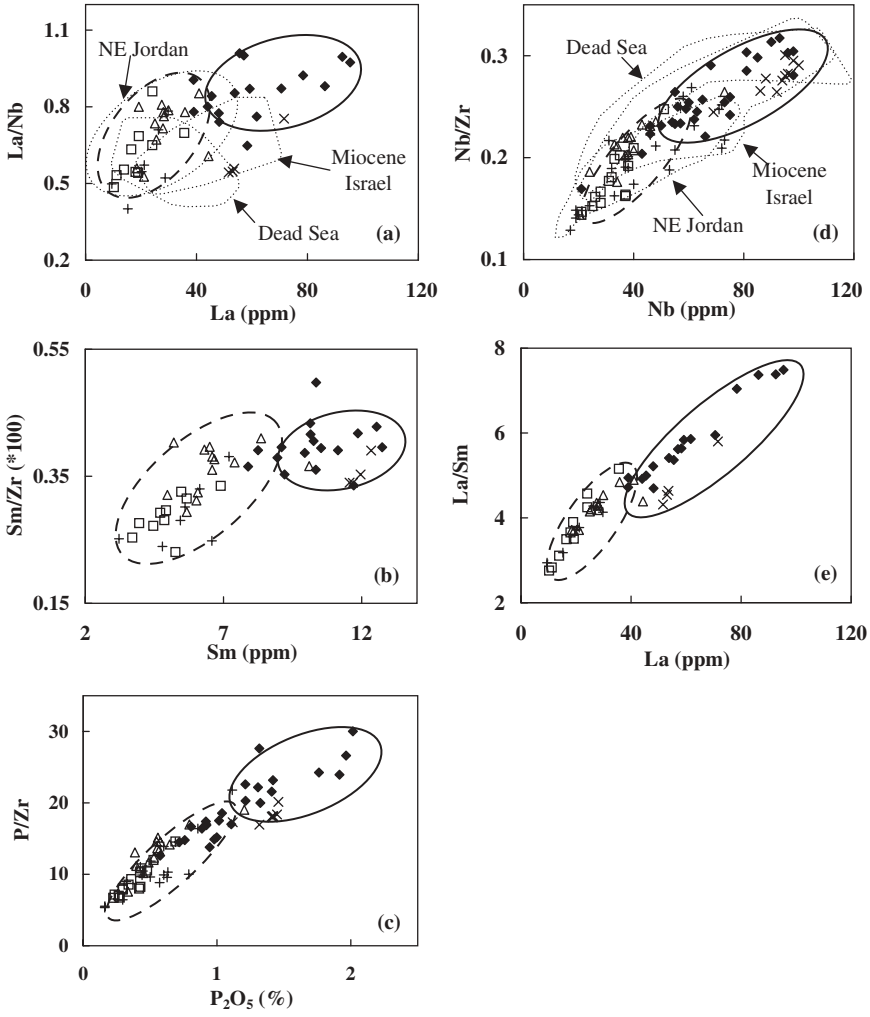

Fig. 7. (a), (b) REE/HFSE vs REE concentration; (c) P/Zr vs wt % P_2O_5; (d) and (e) ratios of highly incompatible to less incompatible elements vs concentration of the highly incompatible element (H/I vs H; see text). Symbols are as in Fig. 2. The field of alkali basalts is encircled by a dashed line and that of basanites by a continuous line. Fields for Miocene basalts from the Yizre'el Valley and southeastern Galilee (Weinstein, 2000) and basalts from northeastern Jordan and the Dead Sea region (Shaw, 2003) are shown in (a) and (d) (a few outliers were excluded in the construction of these fields).

varies between 0·7031 and 0·7034, a composition close to that of PREMA (PREvalent MAntle, Wörner *et al.*, 1986). A similar range of Sr–Nd isotope compositions has been reported for Miocene basalts from the Yizre'el Valley, southeastern Galilee and the southern Golan (εNd 4·1–5·4 and $^{87}Sr/^{86}Sr$ 0·7031–0·7034, Weinstein, 2000; Stein & Hofmann, 1992). The isotopic compositions of the Golan–Galilee basalts fall within the field of basalts from Saudi Arabia (Altherr *et al.*, 1990, Fig. 9a), although the latter show larger ranges in both $^{87}Sr/^{86}Sr$ and εNd (0·7028–0·7035 and 3·6–7·6, respectively), extending towards the Red Sea MORB field (e.g. Volker *et al.*, 1993). Basalts from northeastern Jordan (Shaw *et al.*, 2003) show a significantly wider range of Sr isotope compositions (0·70305–0·70415), whereas their Nd isotope ratios (εNd = 4·1–6·4) are relatively similar to those of the Golan–Galilee basalts. Interestingly, Sr and Nd isotopes are strongly negatively correlated in the Jordanian basalts (Shaw *et al.*, 2003), probably as a result of contamination with an upper crust component. This trend is not observed in the Golan–Galilee and is just slightly shown by the Saudi Arabian basalts (Altherr *et al.*, 1990).

The Sr isotope ratios of the Golan–Galilee basalts are negatively correlated with incompatible element concentrations (e.g. Nb and Sr, Fig. 10a and b) and positively correlated with Rb/Sr ratios (Fig. 10c) and 1/Sr (Fig. 10d).

DISCUSSION

In the following discussion we focus on the nature and the causes of the compositional variability observed in

Table 2: Key element ratios in samples Wy-337 and Wy-16 and averages in the various units

Ratios	Golan Wy-337 alkali basalt	Golan Wy-16 basanite	Golan Early Pliocene	Golan Late Pliocene	Golan Early Pleistocene	Golan Late Pleistocene	Galilee Early Pliocene	Galilee Late Pliocene
La/Yb	5·1	38·7	8·9	13·8	21·3	27·9	10·8	31·4
Tb/Yb	1·71	4·07	1·88	2·44	2·95	3·70	2·33	3·25
Sm/Nd	0·73	0·51	0·65	0·60	0·55	0·53	0·64	0·55
La/Nb	0·50	0·99	0·61	0·70	0·83	0·94	0·56	0·60
Sm/Zr	0·67	1·12	0·74	0·90	0·98	1·08	0·73	0·72
Eu/Ti	0·77	2·07	0·93	1·18	1·39	1·69	1·05	1·09
Rb/Ba	0·49	0·35	0·68	0·49	0·29	0·36	0·40	0·27
Rb/Sr	0·74	0·47	0·75	0·59	0·41	0·46	0·65	0·36
P/Zr	0·78	3·25	1·06	1·56	1·93	2·50	1·09	2·11

Values are corrected to 10% MgO and normalized to Primitive Mantle values (McDonough & Sun, 1995).

the Golan–Galilee basalts. Stein & Goldstein (1996) and Stein *et al.* (1997) have proposed that all Phanerozoic basalts from Arabia have a lithospheric rather than an asthenospheric mantle source. Following this approach, we show below that the compositional variability of the Golan–Galilee basalts reflects the heterogeneous nature of the underlying lithospheric mantle.

Alteration and crustal contamination processes

Alteration probably did not have a significant effect on the chemistry of the Golan–Galilee basalts. Almost all the samples are fresh, showing no petrographic evidence for alteration except for the presence of iddingsite that partially or completely replaces olivine. However, the scatter shown by the Galilee basanites in plots of Rb (and to a lesser extent K) versus SiO_2 (Fig. 4h) or versus other incompatible elements (not shown) implies that this group was subjected to some secondary process that affected the concentration of the more mobile elements. As the Golan basalts show good correlations in the above plots (Fig. 4h) and do not show any other signs of alteration, we chose to focus on this group in the petrogenetic discussion below.

The degree of crustal contamination of the Golan–Galilee basalts, as well as of other Phanerozoic basalts from Israel (Stein & Hofmann, 1992), is probably fairly small on the basis of their Sr and Nd isotope compositions (Fig. 9b). Upper crustal contamination should result in a significantly larger range of variability and higher Sr isotope ratios. A contribution from the lower crust cannot be absolutely ruled out, but should probably result in some variability in Nd isotope composition (Fig. 9b), unlike the uniform values observed in the Golan–Galilee basalts (Fig. 8a). Similarly, Altherr *et al.* (1990) showed that most Saudi Arabian basalts carry near pristine mantle isotopic signatures and ruled out crustal contamination. We note, however, that some Arabian basalts, e.g. from Yemen and especially those from nearby northeastern Jordan, do show a crustal Nd–Sr isotopic signature (Baker *et al.*, 1997; Shaw *et al.*, 2003; Fig. 9a).

Differentiation of the primary magmas

The Golan–Galilee basalts are clearly not primary in composition but are, nevertheless, relatively primitive. Their Mg numbers are between 0·66 and 0·37 (Table 1), MgO contents are usually <12 wt %, and Ni and Cr are <350 ppm and <500 ppm, respectively. This indicates that all the basalts have experienced a certain degree of crystal fractionation. However, most of the incompatible elements show no correlation with MgO concentration (e.g. Fig. 4a–d). This indicates that the wide concentration range of incompatible elements (e.g. a factor of five in Nb and nine in La concentrations) in the Golan–Galilee basalts was not generated by differentiation processes. Rather, the variability in incompatible element concentrations could have originated from mantle source heterogeneity or from variable degree partial melting. The negative correlation of incompatible elements (e.g. Nb, La, Ba, Rb) with SiO_2 (Fig. 4e–h) also supports this conclusion.

Because all of the Golan–Galilee magmas underwent differentiation, their original (primary) incompatible element composition must have been modified to some extent. Based on the good correlation of Ni and MgO (Fig. 3g), we assume that most primitive magmas followed more or less similar differentiation paths. Therefore, to better discuss melting regimes and mantle source compositions, we have corrected the Golan–Galilee basalt compositions to a reference value of 10% MgO by adding various minerals to the bulk-rock composition, following the approach of Klein & Langmuir (1987). This

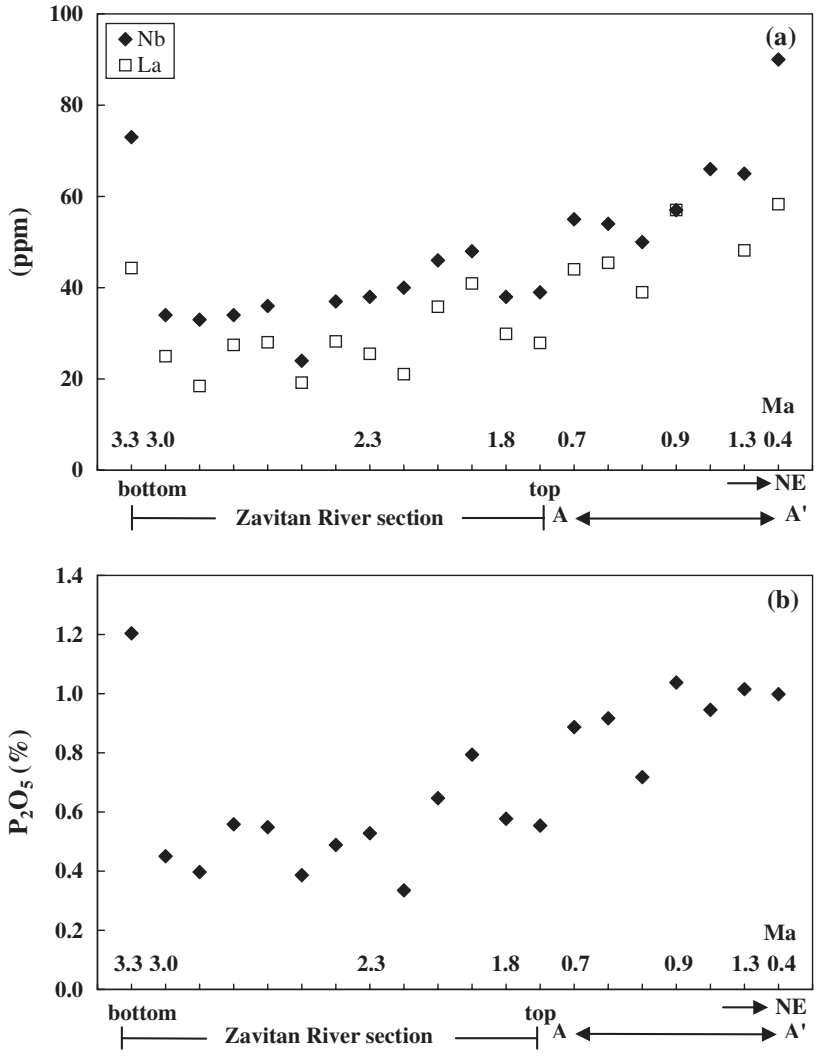

Fig. 8. Concentrations of (a) Nb, La and (b) P_2O_5 in a Plio-Pleistocene section from the central Golan. The section is a combination of (1) a Late Pliocene section (3·3–1·7 Ma, Table 1) taken along the canyon wall of the Zavitan River in the Yahudiya plateau and (2) a Pleistocene section of surface basalts along a line (A–A′, Fig. 1) from the Yahudiya plateau to the NE. The numbers inside the figure are K–Ar ages of some of the samples (in Ma).

correction procedure should restore the magma composition close enough to that of the primary magmas (e.g. Takahashi & Kushiro, 1983; Falloon & Green, 1988). About 10% of the samples have MgO >10% (Table 1, Fig. 3) and required no correction.

The dominance of olivine and clinopyroxene in the phenocryst population and the good correlation of Ni, Cr and Mg numbers with MgO concentrations (Fig. 3a, g and h) suggest that these minerals were the main fractionating phases. Plagioclase fractionation may be ruled out based on the negative correlation between Al_2O_3 and MgO (Fig. 3b), the high Sr concentrations, the rarity of Eu negative anomalies (Fig. 6) and the minor presence of plagioclase phenocrysts in the basalts. Amphibole is also ruled out because of the absence of amphibole phenocrysts. As indicated by the fractionation simulations shown in Fig. 3a, b, d and e, clinopyroxene cannot be the main fractionating phase. On the other hand, olivine alone cannot account for the trend observed in the CaO vs MgO diagram (Fig. 3d) and probably also not for that in the Al_2O_3 vs MgO diagram (Fig. 3b, too steep). Altogether, the data trends are best explained by a fractionating mineral assemblage with an olivine: clinopyroxene ratio of about 60:40, and we use these proportions to correct to 10 wt % MgO. In a few samples, where large deviations from the 60:40 curve were noticed, the proportions were changed accordingly. As the distribution coefficients of both clinopyroxene and olivine are <1 for all incompatible elements, the effect of the

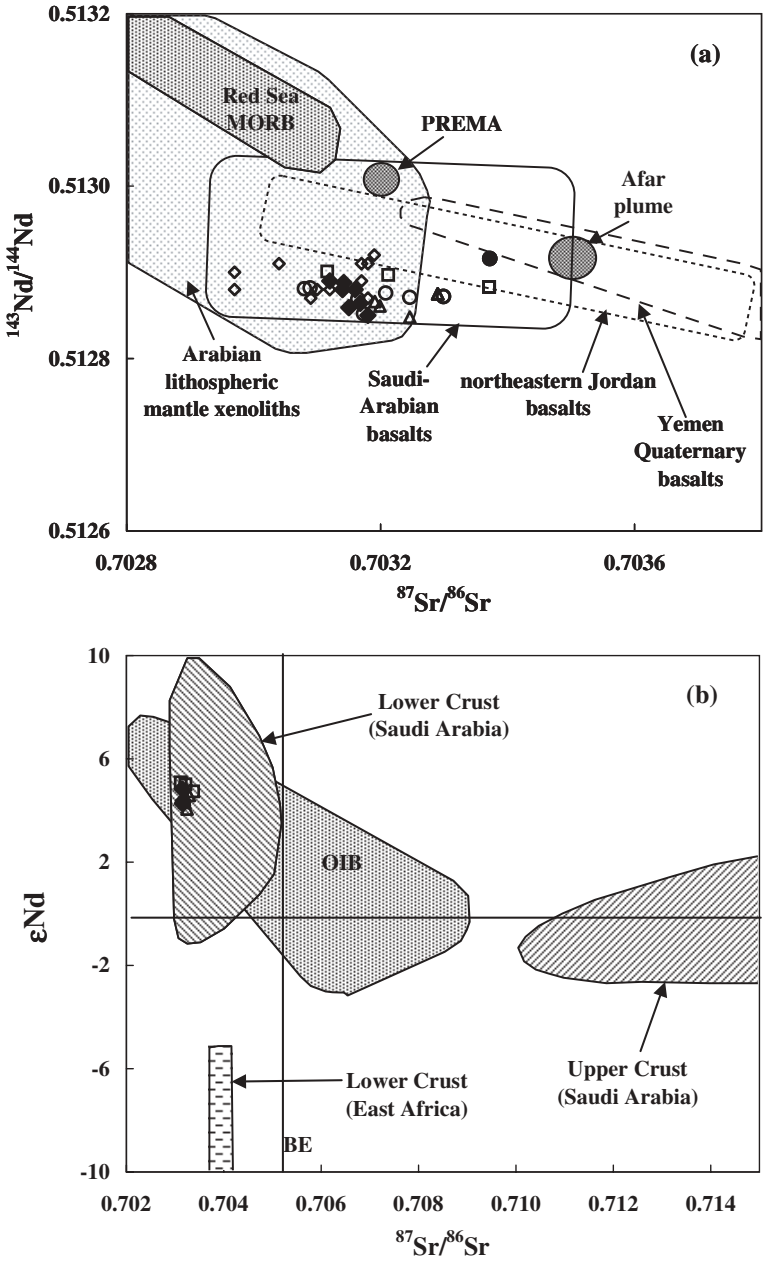

Fig. 9. Sr and Nd isotope ratios in the Golan basalts (including samples from Stein & Hofmann, 1992), Miocene samples from Weinstein (2000) (○, Yizre'el Valley and southeastern Galilee; •, one southern Golan sample) and Mezozoic samples (◇, Stein & Hofmann, 1992). Other symbols are as in Fig. 2. Also shown are: (a) fields of compositions of Red Sea MORB (Hegner & Pallister, 1989; Altherr *et al.*, 1990; Volker *et al.*, 1993; F. Volker, unpublished data, 1994); Saudi Arabian basalts (Altherr *et al.*, 1990); northeastern Jordan (Harrat ash Shamm) basalts (Shaw *et al.*, 2003); Yemen Quaternary basalts (Baker *et al.*, 1997); lithospheric mantle xenoliths from Israel and Arabia (Brueckner *et al.*, 1988; Henjes-Kunst *et al.*, 1990; Stein *et al.*, 1993) and the compositions of PREMA (Wörner *et al.*, 1986) and the Afar Plume (Vidal *et al.*, 1991; Schilling *et al.*, 1992; Deniel *et al.*, 1994); (b) fields of OIB, Arabian lower and upper crust (Duyverman *et al.*, 1982; Cohen *et al.*, 1984; Hegner & Pallister, 1989; Henjes-Kunst *et al.*, 1990; McGuire & Stern, 1993; Stein *et al.*, 1993; O. Gazit, unpublished data, 2005) and East African lower crust (Cohen *et al.*, 1984). BE, Bulk Earth.

correction procedure on the incompatible elements is mainly one of dilution, by up to 17–18% for the highly incompatible elements (e.g. La) and less for others.

The 60:40 ol:cpx ratio assumed in the fractionating assemblage is very different from the usually observed strong dominance of olivine in the phenocryst population of basalts (Table 1). The phenocryst assemblage probably

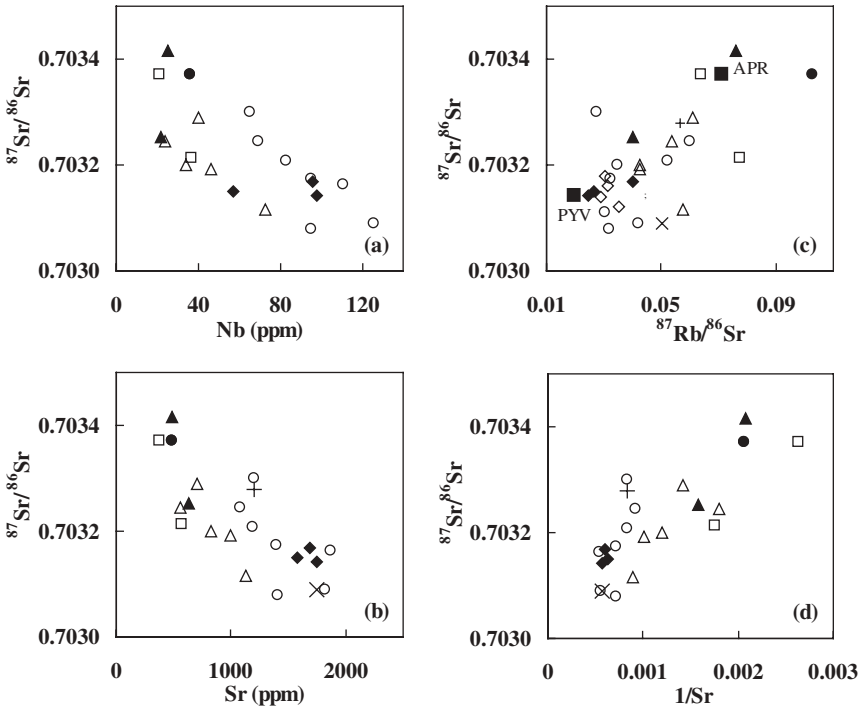

Fig. 10. $^{87}Sr/^{86}Sr$ ratios vs (a) Nb, (b) Sr, (c) $^{87}Rb/^{86}Sr$ and (d) 1/Sr in the Golan–Galilee basalts (symbols as in Fig. 2), including data from Stein & Hofmann (1992), and in Miocene basalts (Weinstein, 2000; symbols as in Fig. 9) and two Late Pliocene to Pleistocene samples from the Korazim area north of the Sea of Galilee (▲, Y. Weinstein, unpublished data, 1998). Also shown in (c) are the compositions of calculated APR and PYV sources (■; Rb/Sr ratios are from Tables 4 and 5, and the $^{87}Sr/^{86}Sr$ values are those of Wy-337 and Wy-52, respectively; see text).

reflects a later, shallower, crystallization stage in which olivine is expected to dominate (e.g. Takahashi & Kushiro, 1983; Sack *et al.*, 1987; Weinstein *et al.*, 1994).

Melting of a heterogeneous lithospheric mantle

On the basis of the above discussion, we consider that the compositional spectrum observed in the Golan–Galilee basalts, especially that of incompatible elements, was not produced by crystal fractionation processes, but reflects mantle source heterogeneity and/or partial melting processes.

Considering the young age of the Golan–Galilee basalts and their low Rb/Sr ratios, the variability of Sr isotope ratios (Fig. 9a) precludes the derivation of the parent magmas from a homogeneous mantle source. Furthermore, the negative correlation of Sr isotope ratios with incompatible element concentrations (e.g. Nb and Sr, Fig. 10a and b) and the positive correlation with $^{87}Rb/^{86}Sr$ and with 1/Sr (Fig. 10c and d) suggest that the spectrum of melt compositions was produced by binary mixing. Mixing is further supported by the upward-convex patterns in some of the H/I vs H diagrams (e.g. Fig. 11a–d) that differ from the linear trends expected in a case of variable degrees of melting (see Hofmann & Feigenson, 1983). The linear trends observed in diagrams of MREE/HREE vs LREE/HREE (e.g. Tb/Yb vs La/Yb, Fig. 11f) also differ from those expected in variable degree of partial melting.

The incompatible element characteristics of the Golan–Galilee basalts (Figs 7 and 11a–e) could alternatively be considered as a combination of two linear arrays, each of which originates from variable degree melting of a distinct mantle source. However, in this scenario we should expect each group to cluster around the $^{87}Sr/^{86}Sr$ ratio of its mantle source. The continuous variation of Sr isotope ratios and their correlation with incompatible element concentrations (Fig. 10a and b) suggests that this is not the case. In addition, it is hard to fit the trace element data with a partial melting model involving two distinct mineralogical assemblages. Source composition and mineralogy that fit a given set of element ratios and concentrations cannot produce the trends of other sets of elements. For example, in the diagram of Nb/Zr vs Nb (Fig. 11a), the relatively moderate trend defined by the more enriched samples (mainly the basanites) is similar (parallel) to the slope of a spinel peridotite melting curve (curve 1 in Fig. 11), whereas the steep slope of the less enriched samples (<40 ppm Nb) is similar to that of a pyroxenite curve (curve 5). On the other hand, in the diagram of La/Nb vs La (Fig. 11b), the trend of the

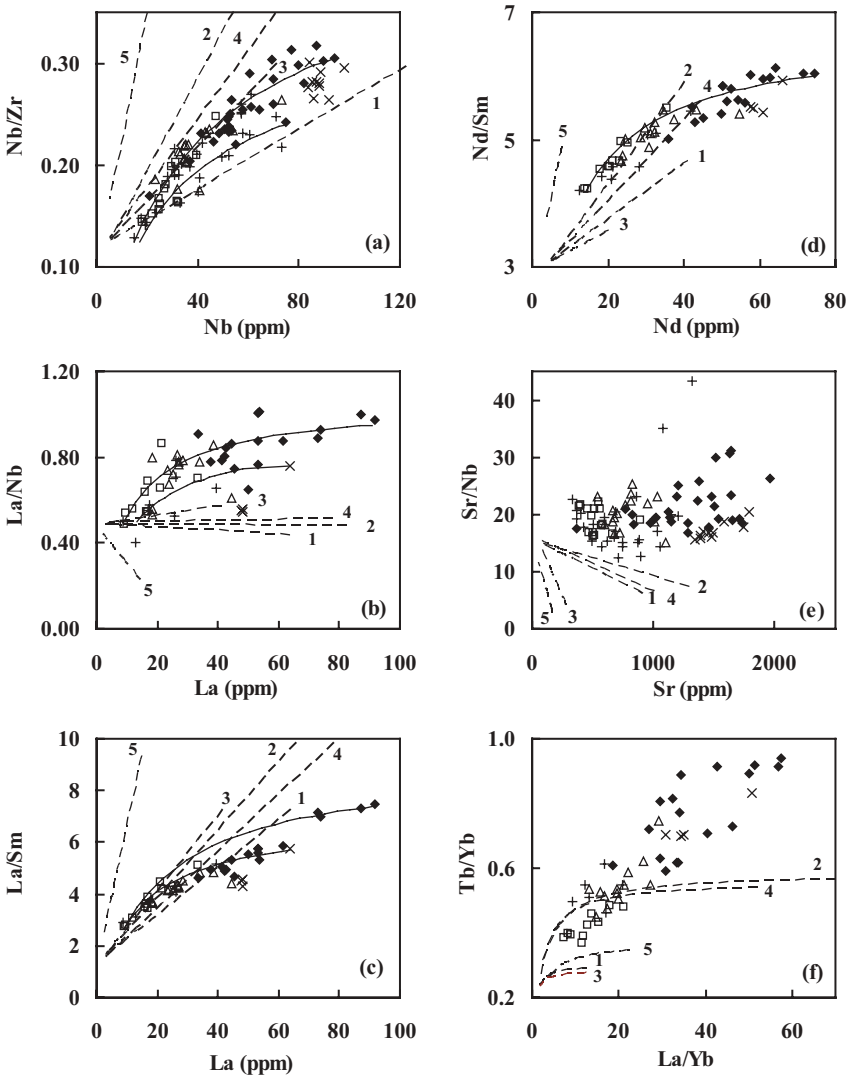

Fig. 11. (a)–(e) Incompatible element ratios vs concentration in the Golan–Galilee basalts. All data are corrected to 10% MgO (see text). Symbols are as in Fig. 2. The fields of alkali basalts and basanites are as in Fig. 7. Also shown are mixing lines (continuous; not numbered) and simulations (dashed curves) of non-modal batch partial melting (Shaw, 1970) in the range 0·1–25% for five source mineralogies: 1, spinel lherzolite (ol:opx:cpx:sp ratios of 60:20:15:5 and −15:50:50:15 in the rock and in the melt, respectively); 2, garnet lherzolite (ol:opx:cpx:gt ratios of 60:20:10:10 and 0:30:35:35 for the rock and melt, respectively); 3, amphibole lherzolite (ol:opx:cpx:am ratios of 55:20:5:20 and −15:35:15:65, respectively); 4, phlogopite–garnet lherzolite (ol:opx:cpx:gt:phl 65:15:10:7:3 and 5:15:60:10:10, respectively); 5, amphibole–garnet clinopyroxenite (cpx:sp:gt:am 75:10:10:5 and 25:20:30:25, respectively). The source composition is arbitrarily assumed to be that of the Primitive Mantle ('PM', McDonough & Sun, 1995), except for Nb, which is assumed to be 2 × PM. Partition coefficients are listed in Table 3. (f) Th/Yb (MREE/HREE) vs La/Yb (LREE/HREE) in the basalts, including mixing lines and batch melting simulations with mineralogies similar to those in (a)–(e) and arbitrarily assuming source La and Tb are 2 × PM, while Yb is 1 × PM. (See text for further explanation.)

enriched samples is similar to that of an amphibole lherzolite (curve 3) or of a phlogopite peridotite melting curve (curve 4), whereas the steeper slope of the alkali basalts could not be produced by any source mineralogy. The opposite is true for La/Sm vs La (Fig. 11c), where the relatively flat slope defined by the enriched samples does not fit any of the melting curves. Moreover, the positive correlation shown by both basanites and alkali basalts in Sr/Nb vs Sr (Fig. 11e) does not match any of the melting simulations. Therefore, we consider that the incompatible element characteristics of the Golan–Galilee basalts are mainly controlled by binary mixing of partial melts from discrete mantle sources, especially in the case of the Golan basalts. Mixing of discrete mantle melts, as opposed to mixing of mantle components (e.g. variable degree of source enrichment), is our preferred model because we anticipate that in the latter the correlation of $^{87}Sr/^{86}Sr$ with incompatible element

concentrations (Fig. 10a and b) would be erased during partial melting processes. Nevertheless, the rarity of reversely zoned phenocrysts in the Golan and Galilee basalts (Weinstein *et al.*, 1994) implies that mixing occurred early in the 'life' of the magma, close to the source area, before the phenocrysts started crystallizing. Mixing as the main control on basalt chemistry was also identified by Shaw *et al.* (2003) in the neighboring northeastern Jordanian basalts.

We therefore conclude that the compositions of the Golan–Galilee basalts reflect mixing of melts derived from two distinct mantle sources. One end-member is the main source for the alkali basalts, and is characterized by relatively low concentrations of incompatible elements, low H/I ratios (e.g. Nb/Zr) and low REE/HFSE HFSE ratios (e.g. La/Nb). The second end-member is enriched in incompatible elements and in the above ratios, and is the main source for the basanites. The compositional range observed in the basanites (e.g. Fig. 11a–c and f) suggests that the enriched source is heterogeneous; namely, it includes a spectrum of enriched compositions.

It is interesting to note that alkali basalts and basanites from the Dead Sea area of Jordan (Shaw, 2003) show a very clear upward-convex trend on a diagram of Nb/Zr vs Nb (Fig. 7d). Miocene basalts from the Yizre'el Valley and the southeastern Lower Galilee (Weinstein, 2000) also show an upward-convex pattern on the same diagram (Fig. 7d). On the other hand, basalts from northeastern Jordan, which were also interpreted in terms of binary mixing by Shaw *et al.* (2003), do show a positive correlation on this diagram but not an upward-convex pattern (Fig. 7d). In all three datasets, an upward-convex pattern is not identified on the La/Nb vs La diagram (Fig. 7a), probably because of the relatively small range of La concentrations in these datasets. However, whereas the Israeli Miocene and the northeastern Jordanian basalts do show a positive correlation (similar to the Golan–Galilee basalts), the Dead Sea samples show a clear negative correlation of La/Nb ratios with La concentrations (Fig. 7a). If the Nb/Zr vs Nb trends (Fig. 7d) are taken as evidence for binary mixing in petrogenesis of the Dead Sea basalts, then the enriched end-member in this case must have had a lower La/Nb ratio than the alkali basaltic end-member.

Unlike Sr isotopes, Nd isotope compositions are uniform in all the Golan–Galilee basalts ($\varepsilon Nd = 4{\cdot}6 \pm 0{\cdot}6$), suggesting a genetic relationship between the two mantle sources. Based on this observation, we suggest that the two mantle sources may have been derived from a common reservoir, which separated into the above two sources. The following discussion focuses on the characterization of the two sources and on their evolution.

Source of the alkali basalts

The melt derived from the alkali basaltic source can be closely characterized by sample Wy-337 from the southern Golan, as it has the lowest concentrations of highly incompatible elements. On a primitive mantle normalized trace element diagram (Fig. 5c), Wy-337 displays prominent peaks at Ba, Nb, Sr, Ti and Zr, and negative anomalies at Rb and U. Because there is no major mantle mineral that can significantly fractionate Rb from Ba, we attribute the low Rb/Ba (Fig. 5a, Table 2) to preferential removal of Rb by hydrous fluids during the petrogenesis of the basalts or the evolution of their mantle sources. Equilibration of the source with fluids may also cause the negative U anomaly (high $D_{(\text{fluid–rock})}$, Keppler, 1996) and the positive Nb anomaly, which as a HFSE has a tendency to be strongly retained in the rock (Keppler, 1996; see Table 3) compared with other elements (including the REE).

The relatively high Sr/Ba and the higher than PM Nb/Ba of Wy-337 (0·71 and 1·10, respectively, PM-normalized ratios) suggest that Ba may have been buffered by a residual hydrous phase. This phase was probably an amphibole rather than a phlogopite, as buffering by phlogopite would cause extremely low Ba concentrations in the partial melts ($D_{\text{Ba(phl-melt)}} > 1$; Adam *et al.*, 1993; LaTourrette *et al.*, 1995), and the Nb/Ba ratio would, therefore, be much higher than that of the primitive mantle. The presence of phlogopite is also not favored by the relatively low K/Nb ratio (<1, PM ratios) in the alkali basalts (Fig. 5a–c).

It is, therefore, suggested that the source for the alkali basaltic end-member melt was an amphibole-bearing peridotite (designated as APR) that underwent partial dehydration, which caused the preferred removal of Rb and U. The presence of amphibole limits the depth of the source to <90 km, as 30 kbar is the maximum pressure for amphibole stability (Green, 1973; Brey *et al.*, 1983; Wallace & Green, 1988). The low Sm/Nd (0·73 PM, Table 2) and the relatively high Tb/Yb (1·7 PM, Table 2 and Fig. 5c) of Wy-337 suggest buffering by garnet, which implies that the APR source was located deeper than 60 km (~20 kbar, Mysen & Boettcher, 1975). Combining the two constraints, the APR source appears to have been located at 60–90 km depth.

A source depth shallower than 90 km implies a lithospheric rather than a deeper mantle origin, as the low heat flow beneath Israel (~40 mW/m^2, Eckstein, 1979) predicts a lithosphere thickness in excess of 100 km. Unlike McGuire (1988), Nasir (1992) and Shaw *et al.* (2003), we consider that the elevated temperatures calculated for peridotitic xenoliths (e.g. 1015°C at 15 kbar in western Arabia, McGuire, 1988; McGuire & Bohannon, 1989; Nasir, 1992; Stein *et al.*, 1993) hosted in Arabian Cenozoic basalts represent local heating by magmas

Table 3: Mineral–melt and fluid–melt partition coefficients used in this study

	ol–m	opx–m	cpx–m	cpx–m*	sp–m	gt–m	gt–m*	amph–m	phlog–m	fl–m
Rb	1·26E − 05	0·0067	0·0058		0	0·007		0·2	2·48	2·7
Ba	1·26E − 05	0·0067	0·0058	0·00032	0	0·0007		0·16	3·68	0·31
Th	2·50E − 05	0·0056	0·014	0·014	0	0·011	0·011	0·0039	0·0014	0·012
U	4·00E − 05	0·015	0·0127	0·0127	0	0·046	0·05	0·0041	0·0011	0·36
K	1·00E − 09	0·0067	0·0072		0	0·22		1·36	4	2·7
Nb	4·10E − 05	0·015	0·0077	0·00081	0·08	0·03	0·0002	0·071	0·088	<0·005
La	1·54E − 05	0·0056	0·0536	0·031	0·0006	0·004	0·0011	0·055	0·028	0·056
Ce	3·60E − 05	0·0058	0·0858	0·061	0·0006	0·02	0·0061	0·096	0·0227	0·056
Sr	0·00012	0·0068	0·1283	0·14		0·002	0·0011	0·298	0·159	0·27
Nd	0·00020	0·007	0·1873	0·14	0·0006	0·1	0·067	0·25	0·012	0·052
P	0	0	0·11	0·05	0	0·15	0·15	0·1	0	0·056
Sm	0·00047	0·0085	0·291	0·21	0·001	0·28	0·35	0·273	0·014	0·052
Hf	0·0046	0·021	0·256	0·14	0·050	0·68	0·27	0·330	0·19	0·005
Zr	0·0013	0·004	0·1234	0·057	0·06	0·4	0·31	0·18	0·017	0·005
Ti	0·009	0·072	0·384		0·15	0·2		0·717	0·98	0·005
Eu	0·00024	0·0078	0·329	0·290	0·001	0·21	0·76	0·297	0·015	0·052
Tb	0·0027	0·011	0·404	0·330	0·001	1·1	1·9	0·42	<0·016	0·052
Yb	0·023	0·032	0·43	0·22	0·005	3·3	11	0·47	<0·020	0·047

m, melt; ol, olivine; opx, orthopyroxene; cpx, clinopyroxene; sp, spinel; gt, garnet; amph, amphibole; phlog, phlogopite; fl, hydrous fluid. References are as follows.
ol–m, Beattie (1994) for Ba, Th and REE (some, by interpolation); Beattie (1993) for U; Kelemen *et al*. (1993) for K; Kennedy *et al*. (1993) for HFSE; *D*(Rb) assumed equal to *D*(Ba); *D*(P) assumed to be zero.
opx–m, Kennedy *et al*. (1993, 1150°C) for most elements; *D*(Rb) = *D*(Ba); *D*(P) assumed to be zero.
cpx–m, mainly Hart & Dunn (1993; some REE, by interpolation); Ba, Th and U from Hauri *et al*. (1994). *D*(Rb) = *D*(Ba); P from Liotard *et al*. (1988).
cpx–m*, *D* values for cpx–m in hydrous melts (10 wt % H_2O), from Green *et al*. (2000); used in Table 5.
sp–m, Stosch (1982) for REE (some, by interpolation); Horn *et al*. (1994) for HFSE; Nielsen *et al*. (1992) for Y; Rb, Ba, Th, U and P assumed to be zero.
gt–m, Van Westrenen *et al*. (1999; values of Py84Gr16) for REE (some, by interpolation), HFSE, Th, U and Sr; Hauri *et al*. (1994) for Ba; Green (1994) for Rb; Thompson (1975) for P.
gt–m*, *D* values for gt–m in hydrous melts (10 wt % H_2O; Green *et al*., 2000); used in Table 5.
amph–m, mainly LaTourrette *et al*. (1995; some REE, by interpolation); *D*(Nb) and *D*(Zr) were corrected to the *D*(Nb)/*D*(La) ratio of Dalpé & Baker (1994).
phlog–m, mainly LaTourrette *et al*. (1995; some REE by interpolation); Ti from Adam *et al*. (1993); *D*(P) assumed zero.
fl–m, 5 M Cl hydrous fluid (Keppler, 1996); REE have very similar low *D* values; therefore, most of them assumed equal to that of Gd (0·052), and Yb equal to Lu; *D*(P) assumed equal to that of La.

(although not the host magmas) and not regional elevated geotherms (see Stein *et al*., 1993).

A lithospheric mantle source for the Israeli and Arabian basalts was previously suggested by Stein & Goldstein (1996), who showed that all juvenile Late Proterozoic magmas from the Arabian–Nubian Shield (ANS) and Phanerozoic alkali basalts from the Arabian plate lie on the same trends in Nd, Sr and Pb isotope evolution diagrams. These trends differ significantly from the growth curves of asthenospheric MORB-source mantle. Moreover, isotope ratios of Israeli Mezozoic basalts (Triassic to Cretaceous) are very similar to those of the Plio-Pleistocene Golan–Galilee ones (corrected initial $^{87}Sr/^{86}Sr$ ratios of 0·7029–0·7031 and εNd of 4·5–5·4, Fig. 9a), probably implying a closer genetic relationship between these two groups than between the coeval Golan–Galilee and Arabian basalts. Stein & Goldstein (1996) concluded that the sources of these magmas have remained associated with the ANS since its formation during the Late Proterozoic Pan-African orogeny and that these sources are, therefore, located in the lithospheric mantle.

Following Stein *et al*. (1997), it is suggested that the incompatible element characteristics of the APR source were acquired during Late Proterozoic Pan-African events as a consequence of fluxing of the newly formed mantle wedge by slab-derived fluids. In the slab, the fluids equilibrated with eclogite and peridotite. In the wedge, a hydration front propagated upwards, leaving behind amphibole peridotite. Trace elements carried

by the fluids partitioned between the fluid and the hydrated peridotite. This chromatographic effect (Navon & Stolper, 1987) led to the stripping of Nb and other trace elements with high *D*(amphibole peridotite–fluid) from the migrating fluid and their preferential retention at deeper wedge levels. Lanthanum and other trace elements with lower *D*(peridotite–fluid) remained in the fluid until shallower wedge levels. As a result, Nb-enriched zones were produced in deeper parts of the wedge, whereas Nb-depleted zones were generated at shallower levels or away from the fluid migration channels. The low La/Nb and Th/Nb ratios of the alkali basaltic melts imply derivation from a Nb-enriched zone.

In Table 4 and Fig. 12 we present a possible model for the petrogenesis of the alkali basaltic Golan end-member (Wy-337). It includes: (1) equilibration of hydrous fluids with a subducting slab (an arbitrary eclogite/peridotite ratio of 1:1 and a fluid/rock ratio of 0·005); (2) infiltration of these fluids and hydration of the mantle wedge, producing amphibole peridotites with Nb-enriched and Nb-depleted zones; (3) partial dehydration of the amphibole peridotite (fluid/rock ratio of 0·005), which significantly reduced, although it did not eliminate, the content of amphibole in the source rock and which caused the large decrease in the Rb content of the source rock; finally, (4) partial melting (~13%), which produced the alkali basaltic end-member melt. Further details of the model can be found in the notes to Table 4.

In summary, the alkali basaltic end-member magmas originated by partial melting of a gt–amph-peridotite (APR). This source composition was formed by Late Proterozoic interaction of peridotite with slab-derived fluids, followed by partial dehydration.

Source of the basanites

For the characterization of the partial melt of the enriched end-member, we used the Golan basanite Wy-16, which is one of the samples with the highest concentrations of highly incompatible elements (Table 1) and the steepest trace element pattern (Fig. 5a and c). However, as mentioned above, the enriched end-member does not have a uniform composition. Therefore, sample Wy-16 does not necessarily represent the exact mixing end-member for all the Golan magmas.

Compared with the alkali basalts, the enriched end-member (Wy-16) has (Table 2):

(1) a stronger negative Rb anomaly (Rb/Ba = 0·35, Rb/Sr = 0·47, PM ratios), which following the above reasoning, implies an intense leaching by fluids;

(2) a negative K anomaly;

(3) a steep LREE–MREE slope (Sm/Nd = 0·5), which suggests either a dominance of clinopyroxene or a major role for garnet in the source;

(4) a very steep MREE–HREE slope (Tb/Yb = 4·2), which implies either a high garnet content in the source or a very low degree of melting;

(5) REE/HFSE ratios higher than those of the alkali basalts (La/Nb approaching unity, compared with 0·5 in Wy-337), which may point to the involvement of a Nb-depleted source;

(6) a positive P anomaly (high P/Nd ratio), which could reflect the dominance of clinopyroxene (phosphorus has a low $D_{(Cpx–melt)}$ compared with its neighboring REE elements, Liotard *et al.*, 1988; see Table 3) or the involvement of apatite.

It is evident that the source for the basanitic melts has to be significantly more enriched than the APR source. In fact, an unreasonably low degree of partial melting (<0·1%) would be needed to produce the Wy-16 La concentration of 134 PM from the APR source. Also, an APR-like source could not produce the very low Rb/Ba of the basanites (Table 2) and the negative K anomaly. To achieve these values, fluid/rock ratios significantly greater than in the case of the alkali basalt source would be required. For example, complete dehydration of an APR source (30% amphibole carrying 1–2 wt % H_2O) would produce a fluid/rock ratio of <0·6%. An external source for the fluids (except for the slab-derived fluids) is rejected, as western Arabia area has been far from any subduction-related plate margin since the Late Proterozoic. Late-stage Rb and K loss during degassing on eruption or secondary alteration is also rejected based on the absence of any correlation between low Rb or K and petrographic evidence for alteration, and the correlation of $^{87}Sr/^{86}Sr$ with Rb/Sr (Fig. 10c), which suggests a mantle source effect. Thus, we conclude that the enriched source was probably rich in clinopyroxene, contained garnet, was highly enriched in incompatible elements (compared with the APR source) and had interacted with a relatively large volume of fluid.

Following the above assumption about a genetic relationship between the two mantle sources, we suggest that the enriched chemical signature observed in Wy-16 and other basanites was generated through a two-stage melting process (Table 5), similar to the process suggested by Francis (1991) and more recently by Thompson *et al.* (2005), as follows. The first stage included the formation of the enriched source by partial melting of an original amphibole peridotite source. During this early melting event, water and other fluids concentrated in the melt. Assuming 1–2% H_2O in the amphibole, 9% melting (Table 5, row 9) while dehydrating 18% of the peridotitic amphibole (see Table 5), we obtain a melt with 2–4% H_2O. This melt then segregated and completely crystallized, forming pyroxenite veins (designated PYV) within the mantle peridotite (Fig. 13). The crystallization depth could be either shallower than or similar to that of the

Table 4: Forward batch melting simulation of production of the alkali basaltic end-member melt (Wy-337)

	Step*	F	Rb	Ba	Th	U	K	Nb	La	Ce	Sr	Nd	P	Sm	Hf	Zr	Ti	Eu	Tb	Yb
	Wy-337 (comp.)†		14·7	27·8	12·21	7·32	23·13	30·5	13·8	14·0	19·7	11·2	9·572	8·12	10·73	12·9	10	7·77	4·62	2·71
11	calculated melt†	13%	16·7	32·3	8·65	6·75	20·4	25·0	13·6	13·1	17·4	11·6	9·5	7·94	7·10	8·7	10·29	8·05	5·30	3·02
10	*P*-melt		0·123	0·097	0·0065	0·0144	0·861	0·051	0·0397	0·071	0·193	0·189	0·107	0·250	0·362	0·201	0·516	0·254	0·514	0·99
9	*D*-melt		0·0264	0·0211	0·0042	0·0079	0·181	0·0164	0·0158	0·0267	0·056	0·0663	0·040	0·098	0·132	0·071	0·177	0·101	0·191	0·368
8	*D*(amph-peridot/fl) (dehydr)†	0·5%	2·35	4·47	1·15	0·92	4·04	3·49	1·91	1·93	2·80	2·00	1·49	1·55	1·53	1·51	2·47	1·59	1·35	1·117
7	*D*(amph-peridot (dehydr)/fl)		0·0098	0·068	0·349	0·02	0·07	3·29	0·282	0·477	0·208	1·27	0·718	1·88	26·49	14·2	35·5	1·9	3·67	7·8
6	amph-peridot comp†		3·54	4·77	1·16	1·12	4·33	3·48	1·94	1·94	2·85	1·99	1·49	1·54	1·52	1·51	2·46	1·59	1·34	1·11
5	*D*(amph-peridot/fl)		0·0206	0·144	0·263	0·0175	0·141	4·66	0·332	0·573	0·326	1·60	0·76	2·00	28·25	15·2	47·6	2·1	3·68	7·0
4	wedge composition†		1	1	1	1	1	1	1	1	1	1	1	1	1	1	1	1	1	1
3	fluid composition†	0·5%	172	33·2	4·43	64·0	30·8	0·75	5·84	3·39	8·75	1·25	1·95	0·77	0·05	0·10	0·05	0·76	0·36	0·16
2	*D*(slab/fl)		0·013	0·086	0·676	0·042	0·093	4·04	0·511	0·885	0·339	2·41	1·54	3·89	55·96	30·4	58·3	4·0	8·26	19·0
1	slab composition†		3	3	3	3	3	3	3	3	3	3	3	3	3	3	3	3	3	3

	Modal (%)	ol	opx	cpx	am	sp	gt
d	melt	0	10	10	60	0	20
c	amph-peridot (dehydr)	48	15	15	12	3	7
b	amph-peridot	48	15	5	27	0	5
a	slab	24	5	36	15	0	20

*The simulation follows the steps from bottom to top, as indicated by the numbers.
†Primitive Mantle (PM) normalized composition.
F, fraction of fluid or melt; fl, fluid; amph-peridot, amphibole peridotites; dehydr, dehydrated.
Notes to Table 4 (following the line numbers):
11. Melt composition calculated using Shaw's (1970) equation for batch melting: $C(\text{melt}) = C(\text{peridot})/\{D + F(\text{melt}) \times [1 - \text{P}]\}$.
10. *P*, partition coefficients using assumed modal proportions in the melt (non-modal melting, line d).
9. *D*(amph-peridotite/melt) values, using modal proportions of line c.
8. Composition of amph-peridotite after dehydration: $C(\text{dehydr peridot}) = C(\text{amph-peridot}) * D(\text{amph-peridot}-\text{fl})/\{F(\text{fl}) + D(\text{amph-peridot/fl}) * [1 - F(\text{fl})]\}$.
7. *D*(amph-peridot(dehydr)/fluid) values, calculated using modal proportions from line c.
6. Amph-peridotite concentrations after equilibration with the slab-derived fluids, calculated as $D(\text{wedge/fluid}) \times C(\text{fluid})$.
5. *D*(wedge/fluid) values, calculated using modal proportions from line b.
4. Wedge composition, assumed to be Primitive Mantle (1 × PM).
3. Concentration in the fluids in equilibrium with the slab, assuming 0·5% *F*−fl. $C(\text{fl}) = C(\text{slab})/\{F(\text{fl}) + D(\text{slab/fluid}) \times [1 - F(\text{fl})]\}$.
2. *D*(slab/fluid) values, calculated using modal proportions from line a and *D*(mineral/fluid) values from Table 3.
1. Primitive mantle normalized (PM) concentrations in the slab, assuming 6 PM in the eclogite and 0 PM in the peridotite.
d. Modal proportions in the melt, assuming non-modal melting.
c. Modal proportions at the end of dehydration.
b. Modal proportions in the wedge amph-peridotite.
a. Modal proportions in the slab, taken as 50:50 eclogite/peridotite ratio.

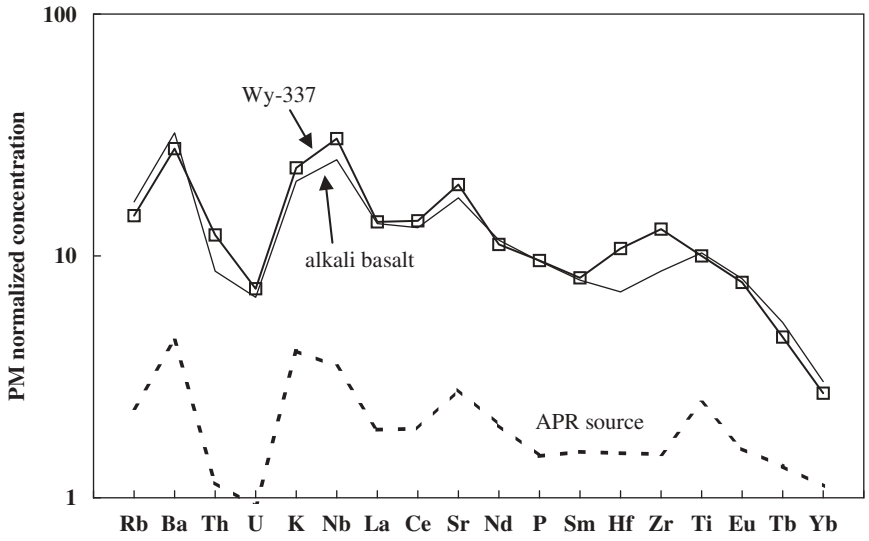

Fig. 12. Primitive Mantle-normalized trace element diagram of the simulated alkali basalt end-member melt, compared with the composition of the alkali basalt sample Wy-337 from the southern Golan (□). Also shown is the composition of the amphibole peridotite source after partial dehydration (APR). (See Table 4 and text for details.)

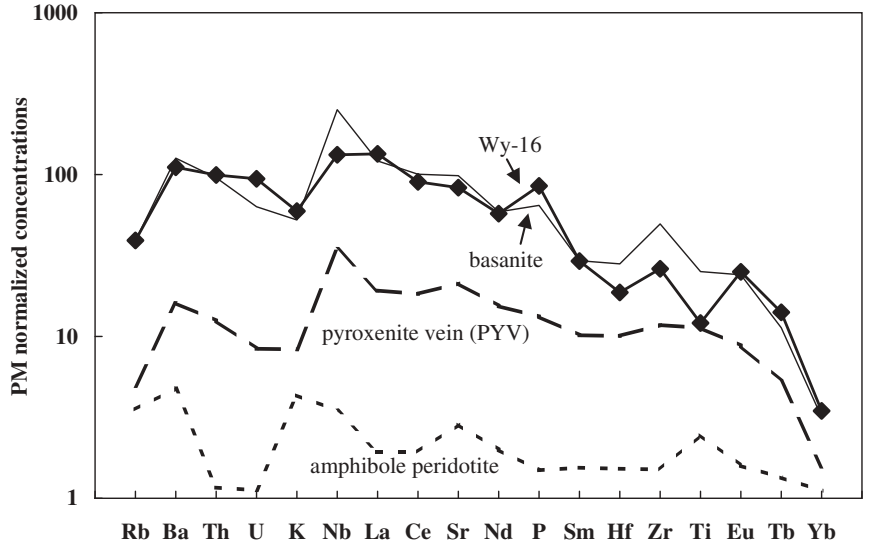

Fig. 13. Primitive Mantle-normalized trace element diagram of the simulated basanitic end-member melt, compared with the composition of the basanite sample Wy-16 (♦). Also shown are the compositions of the amphibole peridotite (no dehydration) and of the pyroxenitic vein source (PYV) after dehydration. (See Table 5 and text for details.)

parental peridotite. Upon crystallization, the melt lost most of its fluids (Table 5, row 11), which preferentially carried Rb and K out of the veins. More recently, during the Plio-Pleistocene, the veins were partially remelted (12%, similar to the APR source) to yield the basanitic end-member magmas (Table 5, row 15; Fig. 13). Upon melting, the magmas equilibrated with neighboring peridotites (Table 5, rows 16 and 17), acquiring close to primary Mg numbers with very little effect on their final trace element composition.

As a fully crystallized H_2O-rich basaltic magma, the veins probably contained some aluminum-bearing phases, e.g. amphibole, spinel and garnet. This is supported by the presence of amphibole pyroxenite xenoliths with variable amounts of amphibole in tuffs from the Golan and spinel- and amphibole-bearing garnet clinopyroxenite xenoliths elsewhere in Israel (e.g. KM-140 with 75% clinopyroxene, 10% garnet, 10% spinel and 5% amphibole; Stein, 1987). Nevertheless, the amphibole content of the pyroxenite source has to

Table 5: Forward simulation of two-stage melting to produce the basanitic end-member melt (Wy-16)

	Steps[1]	F	Rb	Ba	Th	U	K	Nb	La	Ce	Sr	Nd	P	Sm	Hf	Zr	Ti	Eu	Tb	Yb
	Wy-16[2]		39·2	111	99	94	59	132	134	90	83	57·4	85·1	29·2	18·7	26·2	12·1	25·1	14·1	3·47
17	Final melt[2]	0·6	39	126	96	63	52	252	121	101	98	59	65	29	28	50	25·2	24·0	11·3	3·18
16	*D*(peridot/melt)		0·022	0·018	0·003	0·007	0·149	0·014	0·012	0·021	0·044	0·051	0·031	0·075	0·104	0·056	0·144	0·077	0·148	0·291
15	melt 2[2]	12%	39·3	129	96	63·8	59·8	257	123	103	103·5	62·3	67	31·6	31·4	52·9	28·19	25·47	12·4	2·96
14	*P*-melt 2		0·015	0·013	0·012	0·015	0·096	0·017	0·044	0·071	0·112	0·163	0·103	0·260	0·280	0·145	0·355	0·283	0·435	0·68
13	*D*-melt 2		0·007	0·007	0·012	0·013	0·031	0·017	0·041	0·066	0·099	0·147	0·090	0·233	0·234	0·120	0·324	0·258	0·359	0·49
12	residual peridot[2]		0·71	0·77	0·04	0·08	2·85	0·42	0·19	0·32	0·99	0·68	0·32	0·70	0·69	0·51	1·60	0·89	0·96	1·07
11	vein (dehydr)[2]	1·5%	4·93	16·07	12·5	8·39	8·32	34·7	19·2	18·3	21·3	15·4	13·2	10·16	10·06	11·76	11·30	8·76	5·29	1·57
10	*D*(vein/fl)		0·003	0·008	0·959	0·037	0·011	2·16	0·432	0·840	0·397	2·12	0·814	3·40	25·50	13·18	64·7	4·93	6·63	15·3
9	melt (= vein)[2]	9%	32·2	45·2	12·5	11·6	19·2	34·4	19·6	18·4	21·7	15·3	13·3	10·06	9·92	11·60	11·14	8·65	5·22	1·55
8	*P*-melt 1		0·396	0·319	0·0002	0·0003	2·72	0·116	0·094	0·161	0·525	0·429	0·195	0·440	0·572	0·313	1·189	0·448	0·673	0·823
7	*D*-melt 1		0·056	0·044	0·003	0·007	0·380	0·021	0·017	0·030	0·089	0·079	0·040	0·103	0·115	0·068	0·238	0·134	0·228	0·704
6	amph-peridot[2]		3·54	4·77	1·16	1·12	4·33	3·48	1·94	1·94	2·85	1·99	1·49	1·54	1·52	1·51	2·46	1·59	1·34	1·11
5	*D*(amph-peridot/fl)		0·021	0·144	0·263	0·018	0·141	4·66	0·332	0·573	0·326	1·60	0·763	2·00	28·3	15·2	47·6	2·09	3·68	7·01
4	wedge[2]		1	1	1	1	1	1	1	1	1	1	1	1	1	1	1	1	1	1
3	fluid[2]	0·5%	172	33·2	4·43	64·0	30·8	0·75	5·84	3·39	8·75	1·25	1·95	0·774	0·054	0·099	0·0517	0·7622	0·365	0·1587
2	*D*(slab/fl)		0·013	0·086	0·676	0·042	0·093	4·04	0·511	0·885	0·339	2·41	1·54	3·89	56·0	30·4	58·3	3·95	8·26	19·0
1	slab composition		3	3	3	3	3	3	3	3	3	3	3	3	3	3	3	3	3	3

	Modal (%)	ol	opx	cpx	am	sp	gt
f	melt 2	0	5	75	5	5	10
e	amph peridot (resid)	53	17	10	12	3	5
d	vein	0	10	74	1	10	5
c	melt 1	−10	−10	−50	200	−30	0
b	amph peridot	48	15	5	27		5
a	slab	24	5	36	15	0	20

[1]The simulation follows the steps from bottom to top, as indicated by the numbers.
[2]Primitive Mantle normalized composition.
peridot−peridotite; ecl−eclogite.
Notes to Table 5 (following the line numbers):
17. Melt composition after equilibrating with the residual peridotite (rock:melt ratio of 60:40), using *D*'s from line 18.
16. *D*(residual peridotite/melt), using modal proportions of line e.
15. Melt (12%) composition, using Shaw's (1970) equation for batch melting and *D* and *P* from lines 14 and 15.
14. Partition coefficients calculated using melt modal proportions from line f and *D*'s(mineral/melt) from Table 3.
13. *D* (vein/melt), using modal proportions from line d.
12. Composition of residual peridotite (after the 9% melting, see line e).
11. Pyroxenite Vein composition after dehydration [$F(\mathrm{fl}) = 7\%$]; calculation - as in Table 4, line 8.
10. *D* (vein/fluid), using modal proportions from line d.
9. Vein-producing early melting, using Shaw's (1970) equation for batch melting and *D* and *P* from lines 9 and 10.
8. Partition coefficients calculated using assumed modal proportions in the early melt (line c).
7. *D* (amph-peridotite/melt), modal proportions from line b; *D*'s(mineral/melt) from Table 3 [*D*'s of Cpx and Gt are from Green *et al*. (2000)].
6. Amph-peridotite concentrations after equilibration with the slab-derived fluids, calculated as $D(\mathrm{wedge/fluid}) \times C(\mathrm{fluid})$.
5. *D*(wedge/fluid) values, calculated using modal proportions from line b.
4. Wedge composition, assumed to be Primitive Mantle (1 × PM).
3. Concentration in the fluids in equilibrium with the slab, assuming 0·5% *F*−fl. $C(\mathrm{fl}) = C(\mathrm{slab})/\{F(\mathrm{fl}) + D(\mathrm{slab/fluid}) \times [1 - F(\mathrm{fl})]\}$.
2. *D*(slab/fluid) values, calculated using modal proportions from line a and *D*(mineral/fluid) values from Table 3.
1. Primitive mantle normalized (PM) concentrations in the slab, assuming 6 PM in the eclogite and 0 PM in the peridotite.
f. modal proportions in the 2nd stage melt (non-modal melting).
e. modal proportions in the residual amphibole peridotite.
d. modal proportions in the pyroxenitic veins.
c. modal proportions in the 1st stage melt (non-modal melting).
b. modal proportions in the wedge amph peridotite.
a. modal proportions in the slab, taken as 50:50 eclogite/peridotite ratio.

be limited to a few per cent, as a larger fraction would strongly buffer Rb and Ba during dehydration, which would result in higher concentrations of these elements in the final melt. A close fit to Wy-16 composition is obtained using a non-dehydrated amphibole peridotite in the first stage (Table 5, row b) and a pyroxenite in the second stage, composed of 74% clinopyroxene, 10% orthopyroxene, 10% spinel, 5% garnet and 1% amphibole (Table 5, row d).

The calculated vein composition is similar to that of amphibole clinopyroxenite xenoliths found in Pleistocene tuffs from Birket Ram (Golan Heights, Stein, 1987; Stein *et al.*, 1993), which were described by Mittlefehldt (1984) as conduit-filling melts. These xenoliths have Rb/Sr PM-normalized ratios of 0·10–0·17, in close agreement with the ratio of 0·23 for the calculated veins (although the Rb and Sr concentrations in some of these xenoliths are higher than the calculated values by up to a factor of two), and have an $^{87}Sr/^{86}Sr$ isotope ratio of 0·7031, similar to those of the basanites. The Nd isotope ratios of the Birket Ram xenoliths are also very similar to the isotope ratios of the basanites ($\varepsilon Nd = 5{\cdot}1 \pm 0{\cdot}6$ and $4{\cdot}4 \pm 0{\cdot}4$, respectively, Table 1). Pyroxenites from other localities in Israel (Mt. Carmel and Makhtesh Ramon; Stein, 1987) and northeastern Jordan (J. Baker, personal communication, 2005) are less similar to our calculated vein composition and are usually considered to be cumulates from basaltic magmas (Bonen, 1980; Stein, 1987).

The nature of pyroxenite melt compositions has been discussed in a number of studies since the 1960s (e.g. O'Hara, 1968). Kogiso *et al.* (2004), in a recent compilation, concluded that at pressures higher than 2 GPa, the compositions of partial melts of pyroxenites are controlled by the existence of a garnet–pyroxene thermal divide. Silica-excess pyroxenites produce silica-rich melts, whereas melts derived from silica-deficient pyroxenites are silica poor. Kogiso *et al.* (2004) also showed that with increasing degrees of melting, partial melts do not cross the divide. We assume that the composition of the early amphibole peridotitic melt (first stage) was alkali basaltic. Therefore, the resulting pyroxenite veins (PYV) were probably silica deficient, and the second generation melts derived from these veins would, therefore, be silica poor, similar to the basanitic melts. Moreover, according to Kogiso *et al.* (2004), partial melts of silica-deficient pyroxenites tend to have lower silica contents than peridotitic melts, in agreement with the relatively low silica content in the Golan–Galilee basanites.

The two-stage melting scenario explains well the high concentrations of REE in the basanites, while avoiding the need for very low degrees of partial melting, and actually produces both end-member melts by similar degrees of melting (12–13%). The lower U concentration predicted by our model (Fig. 13) is probably the result of our use of the extremely high *D*(fluid–melt) values of Keppler (1996), in which the fluid was a 5 M HCl solution. Values of *D*(fluid–melt) in Cl-free solutions are usually significantly lower, especially for U (0·36 and 0·003, respectively; Keppler, 1996). Using an intermediate value, between those for 5 M HCl and Cl-free solutions, would produce a concentration similar to those in the basanites. Nb concentration in the calculated melt is overestimated (La/Nb in Wy-16 equals 1·0 compared with the calculated value of 0·5; Table 5 and Fig. 13). The lower Nb in the basanites may point to a contribution from a Nb-depleted zone (Stein *et al.*, 1997) during the early melting stage. Contribution from such a depleted zone is probably also the reason for the relatively low concentrations of Zr and TiO_2 in the basanites (Fig. 13). It should be remembered that the enriched end-member is not homogeneous, and some samples (e.g. Wy-292) define a trend toward an enriched end-member with lower La/Nb, which reflects a lower contribution from the Nb-depleted source (Fig. 11b). It is interesting to note that low Nb basalts, which probably originated from Nb-depleted zone, have also been identified in the Dead Sea area (Shaw, 2003; Fig. 7a). An alternative approach to explaining the high La/Nb in the basanites (and the high P concentrations in the basanitic magmas; Table 1) may be the dissolution of apatite (LREE rich and HFSE poor) during the formation of the vein melts.

The presence of some amphibole in the veins, and the suggestion that they were derived from partial melting of amphibole peridotites, places the PYV source within the lithosphere, in agreement with our earlier comment about the uniform $^{143}Nd/^{144}Nd$ ratios and with the suggestion of Stein & Goldstein (1996) that all Phanerozoic Arabian basalts were derived from lithospheric mantle sources. This contrasts with the model proposed by Shaw *et al.* (2003) for the northeastern Jordanian basalts, in which they hypothesized that the enriched magmas (basanites) were derived from an asthenospheric OIB-type source. The main disagreement between the two models concerns lithospheric thickness, and whether or not garnet-bearing mantle rocks are stable at lithospheric pressures. As stated above, in disagreement with Shaw *et al.* (2003) and McGuire (1988), we think that the Arabian–Nubian lithosphere in our study area is thicker than 100 km.

Timing of formation of the two sources

The model developed for the evolution of the sources of the Golan basanites and alkali basalts includes two main stages:

(1) Late Proterozoic subduction-related metasomatism of the Arabian–Nubian lithospheric mantle, which resulted in the formation of amphibole peridotites;

(2) lithospheric differentiation processes, including dehydration and low-degree partial melting of these amphibole peridotites that resulted in the formation of the APR and the PYV sources, respectively.

These events could be related to one of a number of thermal or extension events that the Arabian–Nubian lithosphere has experienced since its formation; these could have occurred either at the end of the Late Proterozoic or at any time during the Phanerozoic. The correlation of $^{87}Sr/^{86}Sr$ with Rb/Sr ratios in the Golan–Galilee basalts (Fig. 10c) cannot be used as an isochron to date these events, as the linear trend observed is interpreted here as a mixing line. However, if the relatively uniform initial Nd isotope ratios (Fig. 9a) of both basanites and alkali basalts are taken as evidence for derivation of their sources from a single mantle protolith, and assuming that both events (dehydration and melting) occurred simultaneously, then the different Sr isotopes compositions of the basanites and alkali basalts could reflect differences in the Rb/Sr ratios of their respective sources acquired during the dehydration and melting processes. Using a two-point model-age calculation for the two sources (PYV and the APR; Tables 4 and 5, Fig. 10c), and using the respective isotopic compositions of Wy-337 and Wy-52 (there are no isotopic data for Wy-16), yields a differentiation age of 313 Ma. Forcing the model source composition to produce melt Rb and Sr concentrations identical to those of Wy-16 and Wy-337 yields older ages (517 Ma). The general slope of the data in Fig. 10c defines an intermediate slope, which, following the same reasoning, yields an age of about 400 Ma. Therefore, we suggest a scenario in which amphibole–garnet peridotites, which were produced in the Late Proterozoic, underwent dehydration and/or partial melting during the Paleozoic, resulting in the formation of the PYV and APR sources. This differentiation event did not produce a large difference in the Sm/Nd ratios of the APR and the PYV sources (0·78 and 0·66, PM-normalized ratios; Tables 4 and 5, respectively), explaining the relative uniformity in the $^{143}Nd/^{144}Nd$ ratios of the basalts.

Although there is no evidence of magmatic activity in the region during Late Paleozoic times, this was nevertheless a period of major uplift and regional erosion (Garfunkel, 1998). A major thermal event in the Israel–Sinai area during the Late Devonian is also implied by zircon fission-track ages (Kohn *et al.*, 1992), K–Ar ages and Rb–Sr isochrons for Cambrian illites (Segev & Steinitz, 1986), and a Nd isotope isochron age of 400 Ma calculated for a suite of pyroxenite xenoliths from northern Israel (Stein, 1987).

Lithospheric mantle heterogeneity

The main message of the above discussion is that the spectrum of compositions in the Golan–Galilee basanites and alkali basalts reflects mixing of melts derived from garnet pyroxenite veins and amphibole–garnet peridotites, respectively. We suggest that the proportion of PYV melt in the mixed product is dependent on the relative proportion of veins in the source; the greater the proportion of veins, the larger the contribution of their melt to the mixed magma and the more enriched the magma is. We, therefore, envisage that the lithospheric mantle beneath northern Israel is composed of several domains that are no more than tens of kilometers in size. The lithospheric domains that supplied the magmas to the southern Golan, as well as to the Lower Galilee, are vein poor, whereas those supplying magmas to the Upper Galilee and to the northern and eastern Golan are vein rich. The Yizre'el Valley, south of the Lower Galilee, was also supplied by magmas from a vein-rich lithospheric domain, albeit at an earlier time (Middle Miocene, Weinstein, 2000). According to our model, the change in magma composition during the Plio-Pleistocene reflects the migration of melting from vein-poor to vein-rich lithospheric domains.

Most of the lavas from the Lower Galilee and southern Golan are compositionally indistinguishable (e.g. Figs 2, 5c and 7). We, therefore, suggest that the southern and western Golan and the Lower Galilee received their magmas from a common vein-poor mantle domain. A single lithospheric domain underlying both the southern Golan and the Lower Galilee is unlikely, as the two regions lie on opposite sides of the Dead Sea Transform, and restoring the 105 km left-lateral displacement along the transform (Freund, 1978) places the southern Golan and its underlying lithospheric mantle at the latitude of Jerusalem, clearly disconnected from the Lower Galilee. We, therefore, propose that both areas were fed by magmas that originated from a vein-poor lithospheric mantle domain in the sub-Golan lithosphere. We prefer the sub-Golan over the Lower Galilee as the source of the magmas for the following reasons. First, in the Golan the APR magmatism continued longer (Early to Late Pliocene) than in the Lower Galilee (Early Pliocene only). Second, the volume of APR magmatism is larger in the Golan, including both the Early Pliocene in the south and the Late Pliocene in the central Golan. This volume may be even larger if the basalts to the south (northern Jordan) and to the east (Syria) are included. Third, the southern Golan lavas are more uniform alkali basalts, whereas those of the Galilee also include more enriched samples (e.g. hawaiites and even one basanite, Fig. 2). It could be that the lithospheric domains to the west of the DST are mainly vein rich, manifested by the Upper Galilee basanites and by the Miocene basanites and nephelinites from the Yizre'el Valley (Weinstein, 2000), and that some of these magmas mixed with sub-Golan-derived APR magmas during the Early Pliocene.

In contrast to the proposed shared APR lithospheric domain, vein-rich domains should be envisaged as isolated pockets, with different compositions under Galilee and under the northern Golan, as suggested by the relatively wide compositional spectrum in diagrams such as La/Nb and La/Sm vs La (see Fig. 11). This is in accordance with the 105 km displacement along the DST, as restoring for the displacement will place these two areas far away from each other.

Cause of Plio-Pleistocene partial melting

The Levant area, including Israel, has experienced several volcanic episodes during the Phanerozoic. These include post-orogenic magmatic activity at the end of the Pan-African period, during the Late Proterozoic to Early Cambrian, and intra-plate basaltic volcanism during the Triassic, the Late Jurassic–Early Cretaceous, the Late Cretaceous and the Neogene–Quaternary (e.g. Garfunkel, 1989). The hydrous nature of the Arabian–Nubian lithospheric mantle, proposed here and elsewhere (e.g. Stein *et al.*, 1997; Baker *et al.*, 1997), is consistent with the common occurrence of hydrous mantle xenoliths in Arabian basalts (e.g. Mittlefehldt, 1984; Stein *et al.*, 1993; Chazot *et al.*, 1996; Downes *et al.*, 2004; J. Baker, personal communication, 2005) and provides a reasonable explanation for these periodic partial melting events, as the wet peridotite solidus is about 300–400°C lower than the dry solidus in the pressure range 20–30 kbar (Fig. 14 and references therein). It is clear from Fig. 14 that under the *P*–*T* conditions of the Arabian lithosphere (Stein *et al.*, 1993), a volatile-saturated lithosphere should be partially molten at pressures in excess of about 25 kbar. Although we cannot disregard the possibility of free volatiles in the source, it is more reasonable to assume fluid-absent conditions (e.g. the H_2O-undersaturated or the CO_2–H_2O-undersaturated solidus curves in Fig. 14). Under such conditions no melting is expected at pressures lower than about 30 kbar. However, lithospheric rocks are very close to their solidus.

The solidus curves illustrated in Fig. 14 are for peridotites. Wet melting experiments are limited to peridotites and there are almost no data for melting of amphibole pyroxenites (the 'veins'). For dry pyroxenites, experimental data show that their solidi are either lower by 50–200°C (Green & Ringwood, 1967; Chapman, 1975; Thompson, 1975) or similar to those of dry peridotites (Ito & Kennedy, 1973; see compilation by Hirschmann & Stolper, 1996). Kogiso *et al.* (2004) have recently demonstrated that pyroxenite solidi are actually higher than those of peridotites with the same alkali contents or Mg-number. However, they noted that, as most pyroxenites have higher alkali contents than peridotites, the actual solidus temperatures of mantle pyroxenites would probably be lower than

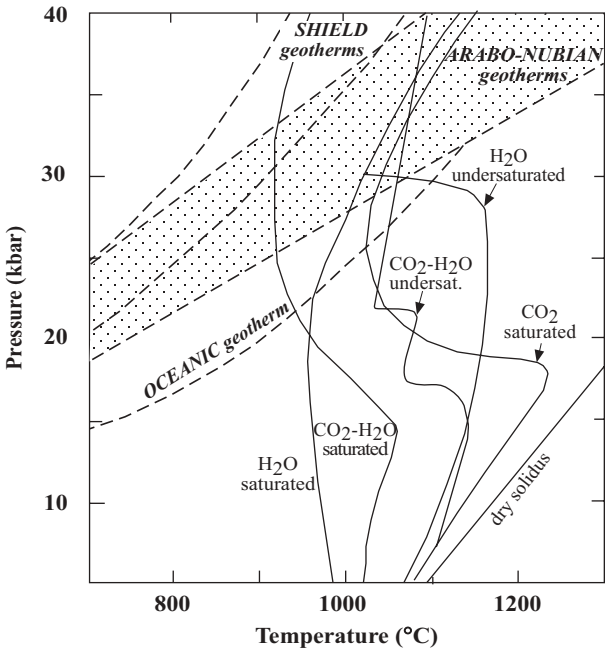

Fig. 14. Geotherms [dashed curves; Falloon & Green (1990) for oceanic and shield geotherms and Stein *et al.* (1993) for that of the Arabian–Nubian massif] and solidus curves (solid lines) of dry and H_2O–CO_2-saturated and -undersaturated peridotites (Green, 1973; Olafsson & Eggler, 1983; Falloon & Green, 1989, 1990).

those of peridotites. Experimental data for phlogopite pyroxenites show that at 20–30 kbar the solidus temperatures are lower than those of phlogopite peridotites (Lloyd *et al.*, 1985; Menner & Dunn, 1995). Therefore, it is probable that the solidus of amphibole pyroxenite is also somewhat lower than that of amphibole peridotite. Nevertheless, in our study we assume similar solidus temperatures for amphibole peridotite and amphibole pyroxenite.

In summary, under the geothermal conditions of the Arabian–Nubian lithosphere, the sources for the Neogene–Quaternary magmas—both peridotites and pyroxenites—were probably close to their solidus, but still within the sub-solidus field. Two mechanisms have been proposed as possible causes for deviation from these conditions to produce partial melting:

(1) decompression as a result of extension (e.g. Bohannon *et al.*, 1989; Stein *et al.*, 1993), associated with rifting along the Red Sea;

(2) thermal perturbation (e.g. Garfunkel, 1989; Camp & Roobol, 1992), possibly in connection with mantle plume activity under Afar, further to the south.

Unlike the Middle Miocene period, when lithospheric extension resulted in the formation of large sedimentary basins throughout the Levant, including the Lower Galilee–Yizre'el Valley (e.g. Shaliv, 1991) and the southern Golan basins, there is no evidence for significant

extension in the region during Plio-Pleistocene times, apart from localized pull-apart basins along the DST. Also, the solidus curves of H_2O- or CO_2–H_2O-undersaturated peridotites are very steep in the pressure range 20–30 kbar (Fig. 14; see also compilation by McKenzie & O'Nions, 1995), throwing doubt on the efficiency of decompression as a major cause for melting in this case. Therefore, we prefer the thermal perturbation scenario. Thermal perturbation means relatively high temperatures in the sub-lithospheric mantle. High temperatures may be caused by a (small) hotspot (Garfunkel, 1989) or by a hot asthenospheric lobe, channeled laterally from the Afar area in the south (Camp & Roobol, 1992), similar to the hot asthenospheric mantle 'fingers' that have been imaged by seismic tomography beneath the volcanic fields of central and western Europe (Granet *et al.*, 1995; Wilson & Patterson, 2001) and postulated to occur beneath the Cenozoic fields of central and northern Africa (Wilson & Guiraud, 1998). Whatever the exact scenario, we suggest that lithospheric melting was caused by heat transferred by conduction from thermally anomalous zone within the sub-lithospheric mantle.

We wish to emphasize that, in our model, partial melting was not triggered or immediately preceded by metasomatic events, as suggested by Bailey (1982) or Wedepohl *et al.* (1994). Instead we propose that the lithosphere was pre-conditioned by metasomatic 'events' that ended hundreds of millions of years earlier (Late Proterozoic). There is no need for introduction of extra-lithospheric fluids and incompatible elements after the stabilization of the lithosphere, as is often suggested for intra-continental alkali magmatism (e.g. Menzies *et al.*, 1987; Menzies & Halliday, 1988; Wilson & Guiraud, 1992) and for kimberlites (Roden & Murthy, 1985). This also means that the recent (Neogene) metasomatism identified by Henjes-Kunst *et al.* (1990) in xenoliths from some Arabian volcanic fields was insignificant in affecting the geochemistry of the mantle sources of Golan–Galilee basalts.

What is the reason for the south–north migration of volcanic activity in the Golan and Galilee? One explanation could be that this is the result of the northward propagation of a hot asthenospheric mantle lobe (e.g. Camp & Roobol, 1992). Alternatively, it could be a mantle source effect, reflecting the location of the vein-rich domains at somewhat shallower depths than the vein-poor domains in the lithospheric mantle, as a result of the early partial melting that probably left a relatively refractory zone at the base of the lithosphere under the vein-rich areas. Therefore, even if sub-lithospheric heating was equally distributed beneath the regional lithosphere, the vein-rich domains, being further away from the heat source, reacted later than the vein-poor domains. The first explanation (the hot asthenosphere propagation scenario) is supported by the fact that vein-rich melting already occurred during the Miocene under the Yizre'el Valley (Weinstein, 2000), to the south of the main Plio-Pleistocene activity. However, the Miocene volcanism could alternatively be the result of the Miocene extension events, which were concentrated in this area (Shaliv, 1991). On the other hand, a scenario of a propagation of a hot asthenosphere lobe cannot be reconciled with the observations from the central Golan, where concentrations of incompatible elements and P_2O_5 increase with time (Pliocene to Pleistocene), although with only a small change in location (about 10 km or less, dependent on where the Pliocene basalts erupted; Fig. 8). Similarly, during the Miocene, most basanites were erupted during the later stages of the period (Weinstein, 2000), as would be expected in the case of shallower vein-rich domains. Therefore, we favor the shallower veins explanation, although the asthenosphere lobe propagation scenario cannot be ruled out.

CONCLUSIONS

(1) The composition of Plio-Pleistocene basalts from the Golan and Galilee, Israel (northwestern Arabia), varies with time and location. Alkali basalts erupted in the south during the Early Pliocene, whereas during the Late Pliocene (west of the Dead Sea Transform) and Pleistocene (east of the transform) magmatic activity was concentrated in the north and was mainly basanitic.

(2) $^{87}Sr/^{86}Sr$ ratios vary between 0·7031 and 0·7034, and correlate negatively with incompatible element concentrations and positively with Rb/Sr ratios. This, together with the upward-convex patterns in plots of incompatible element ratios vs concentration (e.g. Nb/Zr vs Nb, Nd/Sm vs Nd and La/Nb vs La) and other evidence, suggests that the main control on magma composition is binary mixing of melts derived from two end-member sources.

(3) The alkali basalt end-member melt is characterized by relatively high Sr/Ba and Nb/Ba and by low Sm/Nd and relatively high Tb/Yb. Therefore, its source is identified as an amphibole- and garnet-bearing peridotite (APR), limiting its depth to 60–90 km and implying a lithospheric origin for these magmas. The negative anomalies of Rb in the alkali basalts are attributed to a partial dehydration process that shaped the final composition of the APR source.

(4) The basanitic end-member melt is characterized by very high incompatible element concentrations, negative anomalies of K and Rb (the latter stronger than in the alkali basalts), lower Sm/Nd than the alkali basalts and very high Tb/Yb. We propose that these characteristics were produced by a two-stage melting process and that the enriched source of the basanites is pyroxenite veins, hosted by the amphibole peridotites.

(5) The formation of the enriched source of the basanites involves the following stages: (a) early melting of lithospheric amphibole peridotite; (b) solidification of the partial melts to form pyroxenite veins (PYV) within the amphibole peridotites; (c) release of hydrous fluids during solidification of the veins and removal of Rb and K from the veins; (d) Plio-Pleistocene partial melting of the veins (plus reaction with the peridotitic wall-rock) to produce the basanitic end-member.

(6) Based on the above we envisage that the lithosphere beneath northeastern Israel is composed of domains (tens of kilometers scale) that differ in their content of pyroxenite veins.

(7) The uniform $^{143}Nd/^{144}Nd$ ratios may suggest that, in the past, the two sources shared a common source that differentiated by dehydration and partial melting, probably as a result of a Paleozoic thermal event.

(8) Melting during the Plio-Pleistocene probably occurred as a result of heating of the base of the lithosphere by sub-lithospheric, anomalously hot, mantle.

(9) This thermal event migrated from south to north, affecting first (Early Pliocene) vein-poor lithospheric domains and subsequently (Late Pliocene in the Galilee and Pleistocene in the Golan) shallower vein-rich domains.

ACKNOWLEDGEMENTS

This work could not have been accomplished without the help and advice of G. Wörner, who kindly allowed us to use the analytical facilities of the Institute of Geochemistry at the University of Göttingen. We are grateful to the staff of the Geological Survey of Israel, including Y. Mizrahi, S. Ashkenazi, M. Arnon, E. Ram and others who assisted in the field work. The staff of the Institute of Mineralogy at the University of Heidelberg and the Institute of Mineralogy at the Gutenberg University, Mainz, helped in the analytical work. We wish to express special thanks to K. Simon and A. Eisenhauer for their support and technical help, and to A. Heimann for the K–Ar dating. G. Steinitz, Z. Garfunkel, D. Mor, G. Shaliv, A. Rocholl and K. Munker assisted with information and fruitful discussions. Reviews by H. Downes, A. Le Roex and J. Baker were of great help. This study was supported by the Israel Science Foundation (ISF Grant 50399 to M. Stein and Z. Garfunkel).

REFERENCES

Adam, J., Green, T. H. & Sie, S. H. (1993). Proton microprobe determined partitioning of Rb, Sr, Ba, Y, Zr, Nb and Ta between experimentally produced amphiboles and silicate melts with variable F content. *Chemical Geology* **109**, 29–49.

Altherr, R., Henjes-Kunst, F. & Baumann, A. (1990). Asthenosphere versus lithosphere as possible sources for basaltic magmas erupted during formation of the Red Sea: constraints from Sr, Pb and Nd isotopes. *Earth and Planetary Science Letters* **96**, 269–286.

Bailey, D. K. (1982). Mantle metasomatism—continuing chemical change within the earth. *Nature* **296**, 525–530.

Baker, J. A., Menzies, M. A., Thirlwall, M. F. & Macpherson, C. J. (1997). Petrogenesis of Quaternary intraplate volcanism, Sana'a, Yemen: implications for plume–lithosphere interaction and polybaric melt hybridization. *Journal of Petrology* **38**, 1359–1390.

Barberi, F., Capaldi, G., Gasperini, P., Marinelli, G., Santacroce, R., Scandone, R., Treuil, M. & Varet, J. (1980). Recent basaltic volcanism of Jordan and its implications on the geodynamic history of the Dead Sea shear zone. In: Carrelli, A. (ed.) *Geodynamic Evolution of the Afro-Arabian Rift System. Atti die Convegni Lincei* **47**, 667–683.

Bartov, Y., Steinitz, G., Eyal, M. & Eyal, Y. (1980). Sinistral movement along the Gulf of Aqaba (Elat)—its age and relation to the opening of the Red Sea. *Nature* **285**, 220–221.

Beattie, P. (1993). Uranium–thorium disequilibria and partitioning on melting of garnet peridotite. *Nature* **363**, 63–65.

Beattie, P. (1994). What determines the values of mineral–melt partition coefficients? *Mineralogical Magazine* **58A**, 63–64.

Bohannon, R. G., Naeser, C. W., Schmidt, D. L. & Zimmermann, R. A. (1989). The timing of uplift, volcanism and rifting peripheral to the Red Sea: a case for passive rifting? *Journal of Geophysical Research* **94B**, 1683–1701.

Bonen, D. (1980). The Mezozoic basalts of Israel. Ph.D. thesis, The Hebrew University, Jerusalem (in Hebrew).

Bradshaw, T. K., Hawkesworth, C. J. & Gallagher, K. (1993). Basaltic volcanism in the southern Basin and Range: no role for a mantle plume. *Earth and Planetary Science Letters* **116**, 45–62.

Brey, G., Brice, W. R., Ellis, D. J., Green, D. H., Harris, K. L. & Ryabchikov, I. D. (1983). Pyroxene–carbonate reactions in the upper mantle. *Earth and Planetary Science Letters* **62**, 63–74.

Brueckner, H. K., Zindler, A., Seyler, M. & Bonatti, E. (1988). Zabargad and the isotopic evolution of the sub-Red-Sea mantle and crust. *Tectonophysics* **150**(1–2), 163–176.

Camp, V. E. & Roobol, M. J. (1992). Upwelling asthenosphere beneath western Arabia and its regional implications. *Journal of Geophysical Research* **97B**, 15255–15271.

Chapin, C. E. (1979). Evolution of the Rio Grande rift—a summary. In: Rieker, R. E. (ed.) *Rio Grande Rift: Tectonics and Magmatism*. Washington, DC: American Geophysical Union, pp. 1–5.

Chapman, N. A. (1975). An experimental study of spinel clinopyroxenite xenoliths from the Duncansby Ness vent, Caithness, Scotland. *Contributions to Mineralogy and Petrology* **51**, 223–230.

Chazot, G., Menzies, M. & Harte, B. (1996). Determination of partition coefficients between apatite, cpx, amphibole and melt in natural spinel lherzolites from Yemen: implications for wet melting of the lithosphere mantle. *Geochimica et Cosmochimica Acta* **60**, 423–437.

Cohen, R. S., O'Nions, K. R. & Dawson, J. B. (1984). Isotope geochemistry of xenoliths from East Africa: implications for development of mantle reservoirs and their interaction. *Earth and Planetary Science Letters* **68**, 209–220.

Dafny, E., Gvirtzman, H., Burg, A. & Fleischer, L. (2003). The hydrogeology of the Golan basalt aquifer, Israel. *Israel Journal of Earth Sciences* **52**, 139–153.

Dalpé, C. & Baker, D. R. (1994). Partition coefficients for REE between calcic amphibole and Ti-rich basanitic glass at 1·5 GPa, 1100°C. Goldschmidt Conference, Edinburgh. *Mineralogical Magazine* **58A**, 207–208.

Deniel, C., Vidal, P., Coulon, C., Vellutini, P.-J. & Piguet, P. (1994). Temporal evolution of mantle sources during continental rifting: the volcanism of Djibouti (Afar). *Journal of Geophysical Research* **99B**, 2853–2869.

Downes, H., Beard, A. & Hinton, R. (2004). Natural experimental charges: an ion-microprobe study of trace element distribution coefficients in glass-rich hornblendite and clinopyroxenite xenoliths. *Lithos* **75**, 1–17.

Dubertret, L. (1955). The ossiferous seams of Khirbet El Umbachi and of Hebariye (Safa). *Annales Archéologiques de Syrie* **IV–V**, 59–75.

Duyverman, H. J., Harris, N. B. W. & Hawkesworth, C. J. (1982). Crustal accretion in the Pan-African: Nd and Sr isotope evidence from the Arabian shield. *Earth and Planetary Science Letters* **59**, 315–326.

Eckstein, Y. (1979). Review of heat flow data from the eastern Mediterranean region. *Pure and Applied Geophysics* **117**, 150–159.

Falloon, T. J. & Green, D. H. (1988). Anhydrous partial melting of peridotite from 8 to 35 kb and the petrogenesis of MORB. *Journal of Petrology, Special Lithosphere Issue*, 379–414.

Falloon, T. J. & Green, D. H. (1989). The solidus of carbonated, fertile peridotite. *Earth and Planetary Science Letters* **94**, 364–370.

Falloon, T. J. & Green, D. H. (1990). Solidus of carbonated fertile peridotite under fluid saturated conditions. *Geology* **18**, 195–199.

Francis, D. (1991). Some implications of xenolith glasses for the mantle sources of alkaline mafic magmas. *Contributions to Mineralogy and Petrology* **108**, 175–180.

Francis, D. & Ludden, J. (1995). The signature of amphibole in mafic alkaline lavas, a study in the northern Canadian Cordillera. *Journal of Petrology* **36**, 1171–1191.

Freund, R. (1978). The concept of a sinistral megashear. In: Serruya, C. (ed.) *Lake Kinneret. Monographiae Biologicae* **32**, 27–31.

Freund, R., Garfunkel, Z., Zak, I., Goldberg, M., Weissbrod, T. & Derin, B. (1970). The shear along the Dead Sea rift. *Philosophical Transactions of the Royal Society of London, Series A* **267**, 107–130.

Gallagher, K. & Hawkesworth, C. J. (1992). Dehydration melting and the generation of continental flood basalts. *Nature* **358**, 57–59.

Gao, S., Ling, W., Qiu, Y., Lian, Z., Hartmann, G. & Simon, K. (1999). Contrasting geochemical and Sm–Nd isotopic compositions of Archean metasediments from the Kongling high-grade terrain of the Yangtze craton: evidence for cratonic evolution and redistribution of REE during crustal anatexis. *Geochimica et Cosmochimica Acta* **63**, 2071–2088.

Garfunkel, Z. (1981). Internal structure of the Dead Sea leaky transform (rift) in relation to plate kinematics. *Tectonophysics* **80**, 81–108.

Garfunkel, Z. (1989). Tectonic setting of Phanerozoic magmatism in Israel. *Israel Journal of Earth Sciences* **38**, 51–74.

Garfunkel, Z. (1998). Constraints on the origin and history of the Eastern Mediterranean basin. *Teconophysics* **298**: 5–35.

Garfunkel, Z. & Ben Avraham, Z. (2001). Basins along the Dead Sea Transform. In: Ziegler, P. A., Cavazza, W., Robertson, A. H. F. & Crasquin-Soleau, S. (eds) *Peri-Tethys Memoir 6: Peri-Tethyan Rifts/Wrench Basins and Passive Margins. Mémoires du Muséum National d'Histoire Naturelle* **186**, 607–627.

Garfunkel, Z., Zak, I. & Freund, R. (1981). Active faulting in the Dead Sea rift. *Tectonophysics* **80**, 1–26.

Gass, I. G. (1970). Tectonic and magmatic evolution of the Afro-Arabian dome. In: Clifford, T. N. & Gass, I. G. (eds) *African Magmatism and Tectonics*. Edinburgh: Oliver & Boyd, pp. 285–300.

Gazit, O. (2005). Mafic granulite xenoliths from Qarnei Hittin and the evolution of the lower crust beneath northern Israel. *Geological Survey of Israel Report* **GSI/11/05**, 67 pp. (in Hebrew, with English abstract).

Govindaraju, K. (1989). Compilation of working values and sample description for 272 geostandards. *Geostandard Newsletters, Special Issue* **13**, 1–113.

Granet, M., Wilson, M. & Achauer, U.(1995). Imaging a mantle plume beneath the French Massif Central. *Earth and Planetary Science Letters* **136**, 281–296.

Green, D. H. (1973). Experimental melting studies on a model upper mantle composition at high pressure under water-saturated and water-undersaturated conditions. *Earth and Planetary Science Letters* **19**, 37–53.

Green, D. H. & Ringwood, A. E. (1967). The genesis of basaltic magmas. *Contributions to Mineralogy and Petrology* **15**, 103–190.

Green, T. H. (1994). Experimental studies of trace element partitioning applicable to igneous petrogenesis—Sedona 16 years later. *Chemical Geology* **117**, 1–36.

Green, T. H., Blundy, J. D., Adam, J. & Yaxley, J.M. (2000). SIMS determination of trace element partition coefficients between garnet, clinopyroxene and hydrous basaltic liquids at 2–7·5 GPa and 1080–1200°C. *Lithos* **53**, 165–187.

Hart, S. R. & Dunn, T. (1993). Experimental cpx–melt partitioning of 24 trace elements. *Contributions to Mineralogy and Petrology* **113**, 1–8.

Hauri, E. H., Wagner, T. P. & Grove, T. L. (1994). Experimental and natural partitioning of Th, U, Pb and other trace elements between garnet, cpx and basaltic melts. *Chemical Geology* **117**, 149–166.

Hegner, E. & Pallister, J. S. (1989). Pb, Sr, Nd isotopic characteristics of Tertiary Red Sea rift volcanics from the central Saudi Arabian coastal plain. *Journal of Geophysical Research* **94B**, 7749–7755.

Heimann, A. (1990). The development of the Dead Sea rift and its margins in northern Israel during the Pliocene and the Pleistocene. *Geological Survey of Israel Report* **GSI/28/90**, 82 pp. (in Hebrew).

Heimann, A., Steinitz, G., Mor, D. & Shaliv, G. (1996). The Cover Basalt Formation, its age and its regional and tectonic setting: implications from K–Ar and $^{40}Ar/^{39}Ar$ geochronology. *Israel Journal of Earth Sciences* **45**, 55–71.

Henjes-Kunst, F., Altherr, R. & Baumann, A. (1990). Evolution and composition of the lithospheric mantle underneath the western Arabian peninsula: constraints from Sr–Nd isotope systematics of mantle xenoliths. *Contributions to Mineralory and Petrology* **105**, 460–472.

Hirschmann, M. M. & Stolper, E. M. (1996). A possible role for garnet pyroxenite in the origin of the 'garnet signature' in MORB. *Contributions to Mineralogy and Petrology* **124**, 185–208.

Hofmann, A. W. & Feigenson, M. D. (1983). Case studies on the origin of basalt: 1. Theory and reassessment of Grenada basalts. *Contributions to Mineralogy and Petrology* **84**, 382–389.

Horn, I., Foley, S. F., Jackson, S. E. & Jenner, G. A. (1994). Experimentally determined partitioning of HFS- and selected transition elements between spinel and basaltic melt. *Chemical Geology* **117**, 193–218.

Hurwitz, S., Garfunkel, Z., Ben-Gai, Y., Reznikov, M., Rotstein, Y. & Gvirtzman, H. (2002). The tectonic framework of a complex pull-apart basin: seismic reflection observations in the Sea of Galilee, Dead Sea transform. *Tectonophysics* **359**, 289–306.

Ilani, S., Harlvan, Y., Tarawneh, K., Rabba, I., Weinsberger, R., Ibrahim, K., Peltz, S. & Steinitz, G. (2001). New K–Ar ages of basalts from the Harrat Ash Shaam volcanic field in Jordan: implications for the span and duration of the upper-mantle upwelling beneath the western Arabian plate. *Geology* **29**, 171–174.

Ito, K. & Kennedy, G. C. (1973). The composition of liquids formed by partial melting of eclogites at high temperatures and pressures. *Journal of Geology* **82**, 383–392.

Jochum, K. P., Seufert, H. M. & Thirlwall, M. F. (1990). High sensitivity Nb analysis by spark-source mass spectrometry (SSMS) and calibration of XRF Nb and Zr. *Chemical Geology* **81**, 1–16.

Kelemen, P. B., Shimizu, N. & Dunn, T. (1993). Relative depletion of niobium in some arc magmas and the continental crust: partitioning of K, Nb, La and Ce during melt/rock reaction in the upper mantle. *Earth and Planetary Science Letters* **120**, 111–134.

Kennedy, A. K., Lofgren, G. E. & Wasserburg, G. J. (1993). An experimental study of trace element partitioning between olivine, orthopyroxene and melt in chondrules: equilibrium values and kinetic effects. *Earth and Planetary Science Letters* **115**, 177–195.

Keppler, H. (1996). Constraints from partitioning experiments on the composition of subduction-zone fluids. *Nature* **380**, 237–240.

Klein, E. M. & Langmuir, C. H. (1987). Global correlations of ocean ridge basalt chemistry with axial depth and crustal thickness. *Journal of Geophysical Research* **92**(B8), 8089–8115.

Kogiso, T., Hirschmann, M. M. & Pertermann, M. (2004). High-pressure partial melting of mafic lithologies in the mantle. *Journal of Petrology* **45**, 2407–2422.

Kohn, B. P., Eyal, M. & Feinstein, S. (1992). A major Late Devonian–Early Carboniferous (Hercynian) thermotectonic event at the NW margin of the Arabian–Nubian shield: evidence from zircon track dating. *Tectonics* **11**, 1018–1027.

Kramar, U. & Puchelt, H. (1982). Reproducibility tests for INAA determinations with AGV-1, BCR-1 and GSP-1 and new data for 17 geochemical reference materials. *Geostandards Newsletter* **6**, 221–227.

LaTourrette, T., Hervig, R. L. & Holloway, J. R. (1995). Trace element partitioning between amphibole, phlogopite and basanitic melt. *Earth and Planetary Science Letters* **135**, 13–30.

Le Bas, M. J., Le Maitre, R. W., Streckeisen, A. & Zanettin, B. (1986). A chemical classification of volcanic rocks based on the total alkali–silica diagram. *Journal of Petrology* **27**, 745–750.

Liotard, J. M., Briot, D. & Boivin, P. (1988). Petrological and geochemical relationships between pyroxene megacrysts and associated alkali-basalts from Massif Central (France). *Contributions to Mineralogy and Petrology* **98**, 81–90.

Lloyd, F. E., Arima, M. & Edgar, A. D. (1985). Partial melting of a phlogopite-clinopyroxenite nodule from southwest Uganda: an experimental study bearing on the origin of highly potassic continental rift volcanics. *Contributions to Mineralogy and Petrology* **91**, 321–329.

McDonough, W. F. & Sun, S.-S. (1995). The composition of the Earth. *Chemical Geology* **120**, 223–253.

McGuire, A. V. (1988). Petrology of mantle xenoliths from Harrat al Kishb: the mantle beneath western Saudi Arabia. *Journal of Petrology* **29**, 73–92.

McGuire, A. V. & Bohannon, R. G. (1989). Timing of mantle upwelling: evidence for a passive origin of the Red Sea rift. *Journal of Geophysical Research* **94B**, 1677–1682.

McGuire, A. V. & Stern, R. J. (1993). Granulite xenoliths from western Saudi Arabia: the lower crust of the Late Precambrian Arabian–Nubian shield. *Contributions to Mineralogy and Petrology* **114**, 395–408.

McKenzie, D. & O'Nions, R. K. (1995). The source regions of OIB. *Journal of Petrology* **36**, 139–159.

Menner, A. V. & Dunn, T. (1995). Amphibole and phlogopite stability in an initially amphibole-bearing spinel peridotite under water-undersaturated conditions: 1 to 2·5 GPa. *EOS Transactions, American Geophysical Union, Fall Meeting*, 697.

Menzies, M. A. & Halliday, A. (1988). Lithosphere mantle domains beneath the Archean and Proterozoic crust of Scotland. *Journal of Petrology, Special Lithosphere Issue*, 275–302.

Menzies, M. A., Rogers, N., Tindle, A. & Hawkesworth, C. J. (1987). Metasomatic and enrichment processes in lithospheric peridotites, an effect of asthenosphere–lithosphere interaction. In: Menzies, M. A. & Hawkesworth, C. J. (eds) *Mantle Metasomatism*. London: Academic Press, pp. 313–361,

Menzies, M. A., Baker, J., Chazot, G. & Al-Kadasi, M. (1997). Evolution of the Red Sea volcanic margin, western Yemen, In: Mahoney, J. & Coffin, M. (eds) *Large Igneous Provinces: Continental, Oceanic and Planetary Flood Volcanism. Geophysical Monograph, American Geophysical Union* **100**, 29–43.

Mittlefehldt, D. W. (1984). Genesis of cpx–amphibole xenoliths from Birket Ram: trace element and petrologic constraints. *Contributions to Mineralogy and Petrology* **88**, 280–287.

Mittlefehldt, D. W. & Slager, Y. (1986). Petrology of the basalts and gabbros from the Zemah-1 drillhole, Jordan Rift Valley. *Israel Journal of Earth Science* **35**, 10–22.

Mor, D. (1993). A time-table for the Levant volcanic province, according to K–Ar dating in the Golan Heights, Israel. *Journal of African Earth Science* **16**(3), 223–234.

Mysen, B. O. & Boettcher, A. L. (1975). Melting of a hydrous mantle: I. Phase relations of natural peridotite at high pressures and temperatures with controlled activities of water, carbon dioxide and hydrogen. *Journal of Petrology* **16**, 520–548.

Nasir, S. (1992). The lithosphere beneath the northwestern part of the Arabian plate (Jordan): evidence from xenoliths and geophysics. *Tectonophysics* **201**, 357–370.

Navon, O. & Stolper, E. (1987). Geochemical consequences of melt percolation: the upper mantle as a chromatographic column. *Journal of Geology* **95**, 285–307.

Nielsen, R. L., Gallahan, W. E. & Newberger, F. (1992). Experimentally determined mineral–melt partition coefficients for Sc, Y and REE for olivine, orthopyroxene, pigeonite, magnetite and ilmenite. *Contributions to Mineralogy and Petrology* **110**, 488–499.

O'Hara, M. J. (1968). The bearing of phase equilibria studies in synthetic and natural systems on the origin and evolution of basic and ultrabasic rocks. *Earth-Science Reviews* **4**, 69–134.

Olafsson, M. & Eggler, D. H. (1983). Phase relations of amphibole, amphibole–carbonate and phlogopite–carbonate peridotite: petrologic constraints on the asthenosphere. *Earth and Planetary Science Letters* **64**, 305–315.

Omar, G. I. & Steckler, M. S. (1995). Fission track evidence on the initial rifting of the Red Sea: two pulses, no propagation. *Science* **270**, 1341–1344.

Pallister, J. S. (1987). Magmatic history of Red Sea rifting: perspective from the central Saudi Arabian coastal plain. *Geological Society of America Bulletin* **98**, 400–417.

Quennell, A. M. (1958). The structural and geomorphic evolution of the Dead Sea Rift. *Quarterly Journal of the Geological Society of London* **114**, 1–24.

Roden, M. F. & Murthy, V. R. (1985). Mantle metasomatism. *Annual Review of Earth and Planetary Sciences* **13**, 269–296.

Sack, R. O., Walker, D. & Carmichael, I. S. E. (1987). Experimental petrology of alkalic lavas: constraints on cotectics of multiple saturation in natural basic liquids. *Contributions to Mineralogy and Petrology* **96**, 1–23.

Schilling, J.-G., Kingsley, R. H., Hanan, B. B. & McCully, B. L. (1992). Nd–Sr–Pb isotopic variations along the Gulf of Aden: evidence for the Afar mantle plume–continental lithosphere interaction. *Journal of Geophysical Research* **97B**, 10927–10966.

Segev, A. & Steinitz, G. (1986). Dating of epigenetic manganese nodules and reset illites in the Cambrian Timna Formation, southern Israel. Abstracts of the ICOG 6, Cambridge. *Terra Cognita* **6**, *112–113*.

Shaliv, G. (1991). Stages in the tectonic and volcanic history of the Neogene basin in the Lower Galilee and the Valleys. *Geological Survey of Israel Report* **GSI/11/91**, 94 pp. (in Hebrew).

Shaw, D. M. (1970). Trace element fractionation during anatexis. *Geochimica et Cosmochimica Acta* **34**, 237–243.

Shaw, J. (2003). Geochemistry of Cenozoic volcanism and Arabian lithospheric mantle in Jordan. Ph.D. thesis, Royal Holloway University of London, 268 pp.

Shaw, J. A., Baker, J. A., Menzies, M. A., Thirlwall, M. F. & Ibrahim, K. M. (2003). Petrogenesis of the largest intraplate volcanic field on the Arabian plate (Jordan): a mixed lithosphere–asthenosphere source activated by lithospheric extension. *Journal of Petrology* **44**, 1657–1679.

Späth, A., Le Roex, A. P. & Opiyo-Akech, N. (2001). Plume–lithosphere interaction and the origin of continental rift-related alkaline volcanism—the Chyulu Hills volcanic province, southern Kenya. *Journal of Petrology* **42**, 765–787.

Stein, M. (1987). Ultra-basic xenoliths in Cenozoic and Mesozoic volcanic rocks in Israel. Ph.D. thesis, The Hebrew University, Jerusalem, 117 pp. (in Hebrew).

Stein, M. & Goldstein, S. L. (1996). From plume head to continental lithosphere in the Arabian–Nubian shield. *Nature* **382**, 773–778.

Stein, M. & Hofmann, A. W. (1992). Fossil plume head beneath the Arabian lithosphere? *Earth and Planetary Science Letters* **114**, 193–209.

Stein, M., Garfunkel, Z. & Jagoutz, E. (1993). Chronothermometry of peridotitic and pyroxenitic xenoliths: implications for the thermal evolution of the Arabian lithosphere. *Geochimica et Cosmochimica Acta* **57**, 1325–1337.

Stein, M., Navon, O. & Kessel, R. (1997). Chromatographic metasomatism of the Arabian–Nubian lithosphere. *Earth and Planetary Science Letters* **152**, 75–91.

Stolper, E. & Newman, S. (1994). The role of water in the petrogenesis of Mariana trough magmas. *Earth and Planetary Science Letters* **121**, 293–325.

Stosch, H.-G. (1982). REE partitioning between minerals from anhydrous spinel peridotite xenoliths. *Geochimica et Cosmochimica Acta* **46**, 793–811.

Sun, S.-S. & McDonough, W. F. (1989). Chemical and isotopic systematics of oceanic basalts: implications for mantle composition and processes. In: Saunders, A. D. & Norry, M. J. (eds) *Magmatism in the Ocean Basins. Geological Society, London, Special Publications* **42**, 313–345.

Takahashi, E. & Kushiro, I. (1983). Melting of a dry peridotite at high pressures and basalt magma genesis. *American Mineralogist* **68**, 859–879.

Thompson, R. N. (1975). Is upper mantle P contained in sodic gt? *Earth and Planetary Science Letters* **26**, 417–424.

Thompson, R. N., Ottley, C. J., Smith, P. M., Pearson, D. G., Dickin, A. P., Morrison, M.A., Leat, P. T. & Gibson, S. A. (2005). Source of the Quaternary alkalic basalts, picrites and basanites of the Potrillo volcanic field, New Mexico, USA: lithosphere or convecting mantle? *Journal of Petrology* **46**(8), 1603–1643.

Turner, S., Hawkesworth, C., Gallagher, K., Stewart, K., Peate, D. & Mantovani, M. (1996). Mantle plumes, flood basalts and thermal models for melt generation beneath continents: assessment of a conductive heating model and application to the Paraná. *Journal of Geophysical Research* **101B**, 11503–11518.

Van Westrenen, W., Blundy, J. & Wood, B. (1999). Crystal-chemical controls on trace element partitioning between garnet and anhydrous silicate melt. *American Mineralogist* **84**, 838–847.

Vidal, P., Deniel, C., Vellutini, P.-J., Piguet, P., Coulon, C., Vincent, J. & Audin, J. (1991). Changes of mantle sources in the course of a rift evolution: the Afar case. *Geophysical Research Letters* **18**, 1913–1916.

Volker, F., McCulloch, M. T. & Altherr, R. (1993). Submarine basalts from the Red Sea: new Pb, Sr and Nd isotopic data. *Geophysical Research Letters* **20**, 927–930.

Wallace, M. E. & Green, D. H. (1988). An experimental determination of primary carbonatite magma composition. *Nature* **335**, 343–346.

Wedepohl, K. H., Gohn, E. & Hartmann, G. (1994). Cenozoic alkali basaltic magmas of western Germany and their products of differentiation. *Contributions to Mineralogy and Petrology* **115**, 253–278.

Weinstein, Y. (2000). Spatial and temporal geochemical variability in basin-related volcanism, northern Israel. *Journal of African Earth Sciences* **30**, 865–885.

Weinstein, Y., Navon, O. & Lang, B. (1994). Fractionation of Pleistocene alkali-basalts from the northern Golan Heights, Israel. *Israel Journal of Earth Sciences* **43**, 63–79.

White, R. S. & McKenzie, D. (1989). Magmatism at rift zones: the generation of volcanic continental margins and flood basalts. *Journal of Geophysical Research* **94**, 7685–7730.

Wilson, M. & Downes, H. (1991). Tertiary–Quaternary extension related alkaline magmatism in western and central Europe. *Journal of Petrology* **32**(4), 811–849.

Wilson, M. & Guiraud, R. (1992). Magmatism and rifting in western and central Africa, from late Jurassic to recent times. *Tectonophysics* **213**, 203–225.

Wilson, M. & Guiraud, R. (1998). Late Permian to recent magmatic activity on the Afrian–Arabian margin of Tethys. In: MacGregor, D. S., Moody, R. T. J. & Clark-Lowes, D. D. (eds) *Petroleum Geology of North Africa. Geological Society, London, Special Publications* **132**, 231–263.

Wilson, M. & Patterson, R. (2001). Intra-plate magmatism related to hot fingers in the upper mantle: evidence from the Tertiary–Quaternary volcanic province of western and central Europe. In: Ernst, R. & Buchan, K. (eds) *Mantle Plumes: their Identification through Time. Geological Society of America, Special Papers* **352**, 37–58.

Wörner, G., Zindler, A., Staudigel, H. & Schmincke, H. U. (1986). Sr, Nd, and Pb isotope geochemistry of Tertiary and Quaternary alkaline volcanics from West Germany. *Earth and Planetary Science Letters* **79**, 107–119.